01 Dec 2019

Behavior of Hollow-Core Composite Bridge Columns having Slender Inner Steel Tubes

Mohanad M. Abdulazeez

Mohamed ElGawady
Missouri University of Science and Technology, elgawadym@mst.edu

SEISMIC BEHAVIOR OF HOLLOW-CORE COMPOSITE BRIDGE COLUMNS HAVING SLENDER INNER STEEL TUBES

Mohanad M. Abdulazeez and Mohamed A. ElGawady§

Biography:

Mohanad M. Abdulazeez is a Ph.D. Candidate in the Civil, Architectural, and Environmental Engineering Department at the Missouri University of Science and Technology (Missouri S&T), Rolla, MO. He received his BS and MS from the University of Tikrit, Tikrit, Iraq. His research interests include composite materials and seismic behavior of bridges.

ACI member **Mohamed A. ElGawady** is a Benavides Professor in the Civil, Architectural, and Environmental Engineering Department at Missouri S&T. He is the Chair of the Joint ACI-ASCE Committee 441, Reinforced Concrete Columns; current Chair of ACI 341-A, Earthquake Resistant Bridges-Columns; and a member of ACI Committee 341, Earthquake Resistant Concrete Bridges. He received his BS and MS from Cairo University, Cairo, Egypt, and his Ph.D. from the Swiss Federal Institute of Technology (EPFL), Lausanne, Switzerland. His research interests include seismic behavior of concrete and masonry structures, segmental construction, and sustainable material. He won the Missouri University of Science and Technology Research Award in 2018 and Excellence Award in 2017 as well as the American Society of Civil Engineers Innovation Award in 2019.

§Corresponding author

ABSTRACT

This paper experimentally investigates the seismic behavior of two as-built and one repaired hree large-scale hollow-core fiber-reinforced polymer-concrete-steel (HC-FCS) columns. A HC-FCS column consisted of a concrete shell sandwiched between an outer glass fiber-reinforced polymer (GFRP) tube and an inner steel tube. Both tubes provided continuous confinement for the concrete shell along with the height of the column. The columns had two different steel tube diameter-to-thickness (D_s/t_s) ratios of 85, and 254. Each steel tube was embedded into the footing, with an embedded length of 1.25-1.6 times its diameter, while the GFRP tube was not embedded into the footing. Two columns were tested as as-built specimens. Then, one of these columns was repaired and re-tested. This study revealed that HC-FCS columns having a high D_s/t_s ratio of 254 and short embedded length (1.25 D_s) do not dissipate high levels of energy and display nonlinear elastic performance due to severe steel tube buckling and slippage. However, the column with a D_s/t_s ratio of 85 combined with substantial embedment length (1.6 D_s) results in a nonlinear inelastic behavior, high-energy dissipation, and ductile behavior. A repair technique for a high D_s/t_s ratio HC-FCS column precluding buckling of the inner steel tube was proposed and examined. The repair method was characterized by the use of an anchorage system with steel tube concrete filling at the joint interface region. The repaired column achieved the ductile behavior and performed well under seismic loading with flexural strength increased by 22%. However, the lateral displacement capacity decreased by 26% compared to the virgin column due to the residual deformations and stresses exhibited during the previous test.

Keywords: Composite bridge column; Hollow-core; Seismic behavior; Buckling instabilities, Sustainability; Reparability

INTRODUCTION

Americans spend 1.7 million hours/day in traffic congestion due to work zones. [1, 2] Therefore, there is a high demand to reduce on-site construction time and adopt accelerated bridge construction techniques.[3] An excellent candidate for accelerating bridge column construction is the hollow-core steel-concrete-steel (HC-SCS) column, which consists of two generally concentric steel tubes with a concrete shell in between. [4-8] The two tubes act stay-in-place formwork as well as flexural and shear reinforcements, which reduce the workmanship required for steel caging and formwork. HC-SCS also has a high strength-to-weight ratio compared with columns having solid cross-sections. Reducing a column's mass reduces the seismic demand, which would be significant for very tall columns.

Recently, interest has been rapidly growing in using fiber-reinforced polymer (FRP) tubes in different construction applications, including columns. FRP tubes were used, instead of the outer steel tubes, in the HC-SCS columns producing HC-FCS columns.[9-11] The FRP tube increases the ductility of the confined concrete while the use of the inner steel tube is to prevent the inward spalling of the concrete as well as to facilitate connection of the column to the surrounding structural element such as footing. The steel tube is additionally protected from corrosion by both the concrete shell and FRP tube. The concrete shell is confined by both FRP and steel tubes, which results in a triaxial state of compression that increases the strength, ultimate strain, and ductility of the concrete shell. [12, 13]

Experimental [10, 11] and analytical [14] studies have been conducted to investigate the structural behavior of HC-FCS cylinders subjected to axial loads. These studies have generally confirmed the excellent structural behavior of HC-FCSs. The structural performance of HC-FCS cylinders was also compared to that of concrete-filled FRP tubes (CFFTs) and hollow CFFTs. [11] The load versus axial shortening relationship of concrete in HC-FCSs was comparable to that of CFFTs. Furthermore, the inner steel tube prevented the inner concrete spalling, whereas, in the hollow CFFTs, concrete spalling occurred at low strains.

Epoxy-injection technique was extensively applied in the last several decades to fill micro and macro concrete cracks to restore the capacity of seismically damaged reinforced concrete structures with low to moderate level of damage [13, 15-19]. The test results showed improved hysteretic response and ductility of the repaired column, and the epoxy injection was successful in restoring the strength, stiffness, and energy dissipation capacity of the tested specimens.

The diameter-to-thickness ratio of the steel tube (D_s/t_s) in HC-FCSs is crucial for steel buckling. HC-FCS cylinders having inner steel tubes with D_s/t_s ratios ranging from 18 to 90 were investigated under axial loads. [10, 11, 20, 21] While steel tube buckling occurred in these tests and was considered as a critical limit state, none of these studies quantifies the strength or the strain that triggers the occurrence of steel tube buckling.

Few large-scale HC-FCS columns with a low D_s/t_s ratio of 64 - 32 were investigated experimentally under combined axial and lateral loads. [12, 13, 22, 23] The inner steel tubes in these specimens were embedded inside their footings while the GFRP tubes were truncated at the face of the footings. Therefore, the GFRP tubes act as stay-in-place formwork and to provide confinement for the concrete shell. This will allow well-designed HC-FCS columns to behave similarly to under-reinforced well-confined reinforced concrete columns with ductile failure associated with high energy dissipation and damping values. Embedding the GFRP tube in the footing would increase the lateral strength of a HC-FCS column but may result in a brittle failure due to the brittle nature of the GFRP tube. These columns displayed a ductile behavior with high energy dissipation. Furthermore, these studies indicated that failure of HC-FCS columns having steel tubes with low D_s/t_s ratio is triggered by yielding, local buckling of the steel, and then crushing of the concrete.

RESEARCH SIGNIFICANCE

The HC-FCS columns with low D_s/t_s ratios displayed excellent seismic performance. Thus, in order to optimize the HC-FCS column's main component, the steel tube, and to better understand the performance of the columns, this study investigated the seismic behavior of two as-built, and one repaired large-scale HC-FCS columns having an identical cross-section and shear span-to-depth ratio with high D_s/t_s ratios of 85 and 254. Then, one of the columns was repaired and retested under the same loading condition regime. While these values of D_s/t_s ratio seem relatively large, there has been no testing on HC-FCS columns having such high D_s/t_s, ratio and therefore, this data is essential to develop robust analytical and numerical models for HC-FCS columns. The performance of columns having a high D_s/t_s ratio is also of interest for low-to-moderate earthquake-resistant designs where there is relatively low demand on the lateral strength of bridge columns.

EXPERIMENTAL PROGRAM

HC-FCS columns general description

This study investigated the performances of two as-built, and one repaired 0.4-scale HC-FCS columns (**Fig. 1** and **Table 1**) subjected to constant axial load and lateral cyclic displacement. Each column consisted of an outer 610 mm (24 inches) diameter (D_f) filament-wound glass fiber reinforced polymer (GFRP) tube, a 102 mm (4 inches) thick concrete shell, and an inner 406 mm (16 inches) diameter steel tube. The lateral displacement was applied in the middle of a loading head placed atop each tested column at the height of 2,413 mm (95 inches) measured from the top of that column's footing resulting in a shear span-to-depth ratio (H/D_f) of approximately 4. The steel tube's embedded length (L_e) was calculated per **Eq.1**[13] (**Table 1**). The GFRP tube of each column was truncated at the top face of the footing of that column.

$$\frac{D_s t_s f_u}{\left(L_e{}^2\right)} \leq 3.3\sqrt{f'_{c,F}} \tag{1}$$

where f_u is the ultimate stress of the steel tube, and $f'_{c,F}$ is the unconfined cylindrical compressive strength of the concrete footing.

The columns' labels, F4-24-E3(1.5)4, F4-24-E3(0.5)4 and F4-24-E3(0.5)4-R, as used in the current manuscript, consist of a letter, F, in reference to flexural testing, followed by H/D_f (=96/24=4), D_f (=24) in inches, E for the epoxy matrix in the GFRP, the GFRP thickness in multipliers of 3.2 mm (0.125 inches) (=0.375/0.125=3), steel tube thickness in multipliers of 3.2 mm (0.125 inches) (=0.188/0.125=1.5 and 0.063/0.125=0.5), and concrete shell thickness in multipliers of 25.4 mm (1 inch) (=4/1=4). The repaired column is named F4-24-E3(0.5)4-R, where the letter "R" refers to repair.

The steel tube for column F4-24-E3(1.5)4 was available in the market while that for column F4-24-E3(0.5)4 was manufactured out of a steel sheet having the required thickness. The sheet was cut and rolled to the required tube dimensions and then seam-welded using full-penetration groove[24].

Material properties

The average tensile strength of three coupons cut from each steel tube (**Table 1**) and the GFRP tube in the longitudinal direction was determined (**Fig. 2**). The typical GFRP tube used for the three tested columns was 9.5 mm (0.375 inches) thick and the glass fiber was oriented at ±53°. The GFRP tensile properties were found to be relatively close to those reported by the manufacturer's data sheet (**Table 2**). Testing the material properties in the hoop direction was not possible as the diameter of the GFRP tube, 610 mm (24 inches), was quite large.

Self-consolidating concrete [(12)] (**Table 3**) was used for the concrete shells, while conventional concrete was used for the footing (**Table 4**).

Construction and repair procedure

The construction steps for the HC-FCS columns were as follows (**Fig. 1**): 1) Installation of the steel tube inside the footing, 2) Placement of the concrete of the footing, 3) Installation of the GFRP tube and placement of the concrete shell of the column, and 4) Installation of the reinforcement cage and placement of the concrete of the column's head (**Fig. 1 (a)**).

The tested column F4-24-E3(0.5)4 endured severe steel tube buckling localized at the column-footing interface joint and severe steel tube slip. Therefore, repair of this column included injection of a two-component low-viscosity, epoxy liquid, #1001-LV® CPR Products Inc., to fill any micro and macro concrete cracks. The injection process included: 1) sealing the interface joint between the GFRP tube and footing from outside the column using anchoring adhesive (Sika AnchorFix-1). 2) drilling eight 6.35 mm (0.25 inches)-diameter inlet holes through the GFRP and concrete shell without penetrating the steel tube (three on each of the east and west sides where damage was significant during the first test and two on the south side) **(Fig. 3 (a))**. 3) setting the injection ports and injecting the epoxy until it appeared at the next-highest port **(Fig. 3 (b))**. The epoxy injection technique was completed in about 90 minutes. Then, ASTM A307 Grade-A 19 mm (0.75 inches) diameter all-thread galvanized rods were inserted through drilled holes into the HC-FCS column and fastened with two nuts to anchor the steel tube to the concrete shell and GFRP tube minimizing steel slip **(Fig. 3 (c))**. Finally, the bottom 762 mm (30 inches) of the steel tube of that column was filled with concrete to restrain any further local buckling of the steel tube, which was observed during testing the virgin column. After that, a 64 mm (2.5 inches) diameter hole was drilled through the GFRP tube, concrete shell, and steel tube at the height of 762 mm (30 inches) above the footing top level to get an adequate inlet to place concrete. The concrete mix **(Table 5)** was placed using a 51 mm (2 inches) PVC pipe and funnel, located at 1,524 mm (60 inches) above the level of the footing top surface, using the gravity pipe method **(Fig. 3 (c))**. The concrete mix was continuously placed through the funnel until it filled the bottommost 762 mm (30 inches) of the steel tube. A 360-degree camera was inserted inside the column through the drilled hole to monitor the entire repair process. The test was performed three days after the placement of the concrete mix.

Experimental setup and instrumentation

Seventeen linear variable displacement transducers (LVDTs) and string potentiometers (SPs) were used for displacement measurements as following: 1) two SPs for the lateral displacement, 2) eight LVDTs for the vertical displacements along each of the south and north side of the tested columns, 3) three SPs for the relative displacement between the HC-FCS tubes, 4) one LVDT for the footing sliding, and 5) one LVDT for the footing uplift (Fig. 4 (a)). Ninety-six strain gauges were installed on the GFRP and steel tubes at different levels to measure the circumferential and axial strains (**Fig. 4 (b)**). A high-definition webcam was placed inside the steel tube at 635 mm (25 inches) from the top of the footing level to record any inward buckling of the steel tube.

Three SPs were used to measure the slip values between the GFRP tube, concrete shell, and the steel tube. A 19 mm (0.75 inches) diameter hole was drilled through the thickness of each column to the steel tube (**Figs. 4 (c)**) at heights ranging from 254-508 mm (10-20 inches) from the top level of the footing. The SPs were mounted to measure the absolute axial displacements on the GFRP tubes, concrete shell, and steel tube (**Fig. 4 (c)**).

Loading protocol

A constant axial load of 489.3 kN (110 kips) was applied to the column using six external prestressing strands and two servo-controlled jacks that kept the prestressing force constant during testing (**Fig. 5 (a)**). The applied load corresponded to 5% of the axial load capacity of an equivalent RC-column, P_o, having a solid cross-section with the same diameter as the investigated columns and 1% longitudinal reinforcement ratio[25] which is a typical reinforcement ratio in the Midwestern U.S. After applying the axial load, the cyclic lateral displacement [26] (**Fig. 5 (b)**) was imposed using two hydraulic actuators connected to the column loading head (**Fig. 6**). The displacement amplitude a_{i+1} of the step i+1 is 1.4 times the displacement amplitude of the proceeding step of a_i.

RESULTS AND DISCUSSION

The strength, stiffness, as well as energy dissipation capacities of the test specimens, were investigated. The moment-drift (δ) and the average of positive and negative backbone curves of each specimen are shown in **Figs. 7 and 8**, respectively. The drift was calculated by dividing the lateral displacement, measured from the actuators' displacement transducers, by the shear span of 2,413 mm (95 inches). The first yield displacement (δ_y), obtained using the strain gauges on the steel tubes, the displacement δ_u, corresponding to the maximum moment capacity, and the ultimate displacement δ_f at failure for each specimen are summarized in **Table 6**.

Fig. 9 represents the curvature (ϕ) versus the height for each of the tested columns at selected drifts. The average curvature values at different sections along the height of each column were calculated following **Eq. 2** and using the readings of the potentiometers at the column sides.

$$\phi = \frac{\Delta_1 - \Delta_2}{LD} \tag{2}$$

where Δ_1 and Δ_2 are the vertical displacements at the sides of the investigated column, D is the horizontal separation distance between the two potentiometers which were used for measuring the vertical displacements Δ_1 and Δ_2, and L is the vertical gauge length of the potentiometers.

The flexural strengths of the HC-FCS columns were also calculated analytically using Bernoulli–Navier's assumptions and assuming full fixation of the column, elastoplastic model for the steel tube, linear elastic model for the GFRP tube, and Yu et al.'s [27] model for the concrete shell **(Fig. 7)**. More details about the analysis were presented in the relevant literature.[22]

Behavior of the investigated columns

Column F4-24-E3(1.5)4 exhibited stable symmetric hysteresis loops with no visual damage until the end of testing **(Fig. 9)**. The column behaved in a linearly elastic manner, with linear curvature distribution along with the column height until a drift of 1.5% **(Fig. 7 (a))** when the yielding of the steel tube began at the height of 127 mm (5 inches) from the footing face. After yielding, the curvature within the bottommost 254 mm (10 inches) started to increase significantly, reaching 0.0008 (rad/mm) (0.0203 rad/inch) at the end of the test. The strain measurements showed local buckling of the steel tube at approximately 2.2% drift at the interface joint in the south direction of the column **(Fig. 10)**. The column reached its ultimate strength with an average moment capacity of 713 kN.m (526 kips.ft) at a drift of 2.85% **(Fig. 7 (a)),** which was 13% lower than the analytically calculated value of 819.3 kN.m (604 kips.ft). Gradual stiffness degradation occurred beyond a 2.85% drift. Furthermore, a more severe strength and stiffness degradation began at 5.7% drift due to continuous local buckling of the steel tube **(Fig. 11 (a))** and, presumably, concrete cracking near the interface joint, which was observed during the post-test inspection of the column.

While cycling the column to 8.0% drift (**Fig. 7 (a)**), the column displayed a 62% reduction in its strength due to the rupture of the steel tube (**Fig. 11 (b)**) and the test was ended. The post-test inspection of the column showed that permanent steel tube buckling starting at the height of 125 mm (5 inches) above the footing, and extending 254 mm (10 inches) along with the column height. Limited damage to the concrete shell was observed at the bottom 127 mm (5 inches) (**Fig. 11 (c)**) adjacent to the steel tube local buckling location. The concrete footing was intact with no damage observed (**Fig. 11 (d)**).

Column F4-24-E3(0.5)4 exhibited a stable symmetric hysteresis loop with significant pinching due to the minimal steel tube thickness, leading to early buckling of the steel tube near the footing-column interface joint. This buckling deformation was extended gradually downward as noticed through the inside camera, leading to bond deterioration between the embedded steel tube and the surrounding concrete inside the footing, which triggered slippage of the steel tube. The curvature was distributed uniformly along the column length before buckling of the steel tube at 1.1% drift at the interface joint, as verified by the strain measurements (**Fig. 10 (c and d)**). The yielding of the steel tube initiated at a drift of 1.6% at the height of 127 mm (5 inches) from the footing face. The column was able to carry more load beyond yielding of the steel tube and reached its ultimate strength with an average moment capacity of 312 kN.m (230 kips.ft) at 1.8% drift (**Fig. 7 (b)**) which was 24% lower than the analytically calculated value of 407.4 kN.m (300.5 kips.ft) due to early buckling which triggered steel tube slippage. Gradual stiffness degradation occurred beyond the 1.8% drift with more severe stiffness degradation initiated at 5.8% drift due to extensive buckling and slippage (**Fig. 12 (a)**) where buckling extended up to 191 mm (7.5 inches) above the footing top-level at 7.5% drift (**Fig. 12 (b)**). Furthermore, the plastic curvature localized in a region within the bottommost approximately 152.2 mm (6 inches) from the footing top-level (**Fig. 9 (b)**) where the curvature reached 0.00118 (rad/mm) (0.03 rad/inch) at the end of the test. The test was ended at approximately 8.0% drift (**Fig. 7 (b)**) due to excessive slippage with no visual damage to the GFRP tube.

The repaired column F4-24-E4(0.5)4-R showed an improvement in terms of the initial stiffness and hysteresis loops' energy dissipation compared to the virgin column (**Fig. 7 (c)**). Column F4-24-E4(0.5)4-R exhibited asymmetric hysteresis loop with an average moment capacity of 339 kN.m (250 kips.ft) at 1.6% drift, which was 22% higher compared to the as-built column F4-24-E3(0.5)4 (**Fig. 7 (c)).** The reason was due to the improvement in the initial buckling resistance and steel tube slippage because of the internal constraint provided by the concrete infill. The moment capacity was 17% lower than the analytically calculated value of 407.4 kN.m (300.5 kips.ft). Moreover, fatter hysteretic loops were achieved with the repaired column up to 4% drift, indicating more energy dissipation, as discussed later in this manuscript. After that, the pinching effect appeared due to steel tube slippage, which was triggered due to the pre-damage in the steel tube-footing interface during testing of the virgin column. Steel tube tearing was observed at a 6% drift on both the north and south sides (**Fig. 13 (a** and **b))** followed by a drop in bending strength (**Fig. 7 (c)**). No damage in the column's concrete footing was observed (**Fig. 13 (c)**). Concrete infill crushing at the interface joint and slight gradual stiffness degradation occurred beyond that until the end of the test at a 7.9% drift.

Displacement ductility capacity

The idealized bi-linear curve was developed by equating the toughness of the experimental backbone curve to that of the idealized curves (**Fig. 8**). [28, 29] The idealized yield (δ_{iy}) and ultimate (δ_f) displacement obtained from the bi-linear curve were used to calculate the displacement ductility (μ) defined as (δ_f / δ_{iy}), for each column (**Table 4, Fig. 8)**. The initial idealized stiffness, $K_i = F_{iy}/\delta_{iy}$ where F_{iy} is the idealized lateral force correspondent to δ_{iy} **(Table 4),** for column F4-24-E3(1.5)4 was 42.67, slightly higher by 3% than that of column F4-24-E3(0.5)4 with K_i of 41.5. The repaired column F4-24-E3(0.5)4-R was highly improved in terms of the initial stiffness and displayed K_i of 47, which was 12 % higher than the virgin column.

All three columns displayed an acceptable level of ductility exceeding a displacement ductility capacity of 5 required for a single column in SDC D for AASHTO guide specifications for LRFD seismic bridge design. [30] Column F4-24-E3(1.5)4 reached a μ of 5.4 while columns F4-24-E3(0.5)4, and F4-24-E3(0.5)4-R displayed μ values of 12 and 9.23, respectively. However, the μ values for columns F4-24-E3(0.5)4 and F4-24-E3(1.5)4-R should be interpreted carefully as they occurred mainly due to tube slippage with limited energy dissipation.

Lateral stiffness degradation

Stiffness degradation is a crucial element for nonlinear modeling of structures. In HC-FCS columns, this degradation can be attributed to the buckling and slippage of the steel tube, GFRP tube rupture, if any, and concrete shell's cracking and crushing. In this study, the secant stiffness (K_{sec}), defined as the column stiffness for a given loading loop using the peak displacement and corresponding lateral load of that loop,[31] normalized by the yield stiffness $K_y = F_{iy}/\delta_{iy}$, was used as the stiffness degradation parameter (**Fig. 14**). As shown in the figure, the stiffness degradation of all test columns was similar in the trend. Moreover, the columns F4-24-E3(0.5)4 and F4-24-E3(0.5)4-R were 15% less than column F4-24-E3(1.5)4 due mainly to the steel tube with high D_s/t_s as well as insufficient L_e.

Steel strains

Based on the test results, the D_s/t_s affected the performance of the steel tubes in HC-FCS columns. **Fig. 15 (a)** shows the steel tube buckling-to-yield strain ($\varepsilon_b/\varepsilon_y$) versus D_s/t_s ratios of the investigated as-built columns. **Fig. 15 (b)** shows the ultimate (rupture)-to-the first buckling drift (δ_r/ δ_b) versus D_s/t_s of the tested columns. F4-24-E3(1.5)4 exhibited steel yielding followed by local buckling (**Fig. 15**). **Fig. 10** shows an example of the axial steel tube strains at the interface joint versus drift for the F4-24-E3(1.5)4 column. The steel tube yielded at approximately 1.5% drift and then buckled at a 2.2% drift. Beyond that, the steel tube reached a 7,164 microstrains at 2.5% drift on the north side, where the column reached its peak strength. Upon further loading at 3.25% drift, local buckling was highly localized at the interface joint. Subsequently, local cyclic fatigue triggered a fracture of the tube in the buckled section (**Fig. 11 (a)**). The fracture propagated and was observed visually at 8.1% drift through the section, accompanied by a noticeable loss of flexural capacity in the hysteretic response (**Fig. 11 (a))**. The hoop strains showed that the tube was under continuous contraction, reaching a strain of 1,600 microstrains at approximately +/- 8% drift (**Fig. 11 (b)**).

The steel tube at the interface joint of F4-24-E3(0.5)4 buckled at approximately 1.1% drift followed by yielding at approximately 1.5% drift (**Fig. 15** and **Fig. 11 (c and d)**). The steel tube reached an axial strain of approximately 3,800 microstrains at 1.6% drift on both sides, where the column reached its peak strength. Beyond that, the axial strains dropped, and the column strength started to degrade until the end of the test. The tube contracted in the hoop direction during testing, and the hoop strains remained within 600 to 1,000 microstrains up to 4% drift (**Fig. 11 (c and d)**).

GFRP strains

The vertical strain in the GFRP tube of F4-24-E3(1.5)4 on the north side reached approximately 10,880 microstrains at 8% drift (**Figs. 16 (a) and 17 (a)**) at 127 mm (5 inches) above the top footing level. After that, the strain reading decreased by 20% at the same drift due to the rupture in the steel tube. While on the south side, a strain concentration at 127 mm (5 inches) above the footing top level and the axial strain reached an approximate value of 6,000 microstrains at 4% drift at (**Fig. 16 (b))**. Beyond that, the column strength decreased (**Fig. 7 (a)**), resulting in a reduction in the GFRP axial strains and also releasing in the strain concentration at the 127 mm (5 inches) column height. The peak strain located at the interface of the column-footing and reached a maximum value of 6,500 microstrains at the drift of 8 % on the south side (**Fig. 16 (b)**).

The GFRP tube of the F4-24-E3(1.5)4 column had reached an ultimate hoop tensile strain of 8,400 (**Fig. 16 (c and d)**), which was 230% higher than that of 3,650 microstrains obtained for F4-24-E3(0.5)4 column at 6% drift. The high strains were within the bottommost 203-254 mm (8-10 inches) for all of the columns. It is worth mentioning that the strain profile readings of the F4-24-E3(0.5)4 column reached approximately zero at 508 mm (20 inches) above the footing top-level, indicating that the GFRP upper part of the column endured no stresses during the lateral cyclic loadings (**Fig. 16 (e)**), which is attributed to the insufficient L_e that required to maintain the flexural behavior for the whole system. **Fig. 17 (a and b)** represents the GFRP tube's vertical and horizontal strain readings versus drift hysteresis curves for column F4-24-E3(1.5)4 at the interface joint. As shown in the figure, the vertical strain readings on the north side reached a compression value of approximately 14,700 microstrains, which is 23% less than the rupture strain.

The repaired column F4-24-E3(0.5)4-R showed a considerable hoop strain value of 7,200 microstrains, which was approximately 100% higher than the virgin column. The reason was due to the presence of the inside concrete infill diminishing the steel tube‘s inward buckling and thereby helping the GFRP tube to provide more confinement for the concrete shell.

Furthermore, the hoop strains up to a 3.2% drift showed nonlinear elastic behavior with minimal strain values developed in the GFRP tube, indicating minimal concrete dilation and microcracks. Beyond that, and due to the severe dilation in the concrete shell, the strains in the GFRP tube significantly increased when increasing the applied lateral displacement. However, once the applied lateral displacement was reversed, the circumferential strains decreased but did not fully recover, indicating permanent concrete dilation and microcracks. At 2.8% drift, the column reached its peak strength with a peak hoop strain of 4,200 microstrains and a residual hoop strain of 1,400 microstrains. At the end of the test, the hoop strains reached 14,700 microstrains, representing 77% of the tube failure strain with a 9,000 microstrains residual strain. Column F4-24-E3(0.5)4 behaved similarly to column F4-24-E3(1.5)4. However, the hoop strain at the test end reached approximately 4,200 microstrains with a 2,700 microstrains residual strain. These strain values were 59% and 66% less than what was obtained with column F4-24-E3(1.5)4. This reduction in the hoop strains occurred as the concrete dilated toward the very thin steel tube in the case of column F4-24-E3(0.5)4 with high D_s/t_s of 254 compared to column F4-24-E3(0.5)4 with D_s/t_s of 85.

The horizontal strain readings on the north side reached a tensile value of approximately 14,700 microstrains, which was 150% larger than on the south side at 8% drift (**Fig. 17 (b)**). The reason was due to the steel tube buckling that generated on the south side (**Fig. 12 (b)**), thereby releasing (decreasing) the pressure of the compressed concrete on the GFRP tube at the interface joint.

Fig. 17 (c and d) represent the GFRP tube vertical and horizontal strain readings versus drift hysteresis curves for column F4-24-E3(0.5)4 at the interface joint. As shown in the figure, the vertical strain readings on the south side reached a compression value of approximately 4,000 microstrains at an 8% drift. Furthermore, the horizontal strain readings on the north side reached a tensile value of approximately 4,200 microstrains on both sides at an 8% drift. The reason was due to the early steel tube slippage because of the L_e efficiency and thereby low hoop strain values at the joint interface region. It is interesting to note that all the hoop strains in **Fig. 17** are positive (i.e., tensile), suggesting that the concrete was significantly confined in both the compression and the tension zones of the column section at the interface joint. Moreover, increasing the D_s/t_s of the as-built columns by 300% from 85 for column F4-24-E3(1.5)4 to 254 for column F4-24-E3(0.5)4 decreased the hoop strain by 71% from 14,700 to 4,200 microstrains for the same columns due to less confinement pressure obtained for the concrete shell.

Fig. 17 (e and f) represents the GFRP tube vertical and horizontal strain readings versus drift hysteresis curves for column F4-24-E3(0.5)4-R at the interface joint. As shown in the figure, the vertical strain reading on both the north and south sides reached a compression value of approximately 10,000 microstrains at 8% drift, while the horizontal strain was 7,000 microstrains at the south side. The reason for these relatively high readings for the repaired column was due to the presence of the all threaded anchored bars that highly restrained the GFRP at a level of 127-254 mm (5-10 inches), acting like a ring confining the GFRP on all sides and squeezing it to the concrete infill inside the steel tube.

Plastic hinge length

Plastic hinge length is crucial in the seismic design analysis of a bridge column. The height, L_p, where the hoop strain value on the GFRP drops to one-third of its peak value, was proposed [32] as the plastic hinge length of a CFFT column. Using this approach, the envelope of the hoop strain

(**Fig. 18)**, L_p values were calculated as 150 mm (5.9 inches) and 135 mm (5.3 inches) for columns F4-24-E3(1.5)4 and F4-24-E3(0.5)4, respectively (**Fig. 18 (a and c))**. Furthermore, the curvatures along the heights of the columns displayed significant changes in their values (**Fig. 18 (b and d))** at 165.1 mm (6.5 inches) and 152 mm (6 inches) above the footing of columns F4-24-E3(1.5)4 and F4-24-E3(0.5)4, respectively, indicating that the plastic hinges occurred within these lengths. These lengths obtained were approximately 11% higher than those obtained based on the GFRP hoop strains criterion.

Slip of the different components of the columns

For column F4-24-E3(1.5)4 (**Fig. 19 (a)),** the relative movement between the steel tube and concrete shell, as well as between the steel tube and GFRP, were measured using two SP (**Fig. 4**). Furthermore, the interface joint between the GFRP tube and footing was measured using another SP (**Fig. 4**). As shown in **Fig. 19 (a)**, there was no slip between the different tubes. Moreover, the joint opening (*JO*) increased linearly with an increase in the applied drift. The joint opening reached 61 mm (2.45 in) at the drift of 11%. The *JO* resulted from the slip of the inner steel tube and elongation in the embedded length of the steel tube.

For column F4-24-E3(0.5)4 (**Fig. 19 (b)**), the SP that measured the slip between the steel tube and GFRP malfunctioned. However, there was a significant slip that took place between the GFRP and concrete shell, reaching 11.4 mm (0.45 in.) at a drift of 7%. As explained earlier, there is an interaction between the concrete shell lateral dilation direction and the relative stiffness of the GFRP and steel tubes. In the case of column F4-24-E3(0.5)4, since the steel tube had a high D_s/t_s, concrete dilated toward the steel tube and hence displayed more substantial slippage between the concrete shell and GFRP tube. Moreover, the *JO* values for column F4-24-E3(1.5)4 were lower than those of column F4-24-E3(0.5)4. At 8% drift, the *JO* of column F4-24-E3(1.5)4 was 22% lower than that of column F4-24-E3(0.5)4. The larger *JO* values were attributed to the excessive slip that took place during testing column F4-24-E3(0.5)4.

Energy dissipation (E_d)

The dissipated energy of the investigated columns was calculated as the difference between the input energy and elastic energy. The cumulative energy dissipation was calculated by adding the values of energy dissipated during the first cycle of each loading displacement. All columns dissipated the same amount of energy until a drift of approximately 2% (**Fig. 20).** Beyond that, column F4-24-E3(1.5)4 dissipated the highest amount of energy followed by columns F4-24-E3(0.5)4-R and F4-24-E3(0.5)4, respectively. At 7.8% drift, column F4-24-E3(1.5)4 dissipated energy 230% and 330% higher than the F4-24-E3(0.5)4-R and F4-24-E3(0.5)4 columns, respectively. A major portion of the energy dissipation in these columns occurred when the inner steel tubes underwent large plastic deformations, which occurred after an approximately 1.5-1.8% drift. Column F4-24-E3(0.5)4 displayed the lowest amount of energy dissipation due to the high D_s/t_s ratio of 254 and the significant slip during testing. Furthermore, column F4-24-E3(0.5)4-R was able to dissipate energy higher than the as-built F4-24-E3(0.5)4 column, which indicated the capability of the repair technique to prevent the inward steel tube buckling and to reduce the slip and hence trigger more plastic deformations and higher energy dissipation.

Equivalent viscous damping

The equivalent viscous damping, ζ, which is crucial for seismic analysis, was calculated for the tested columns, per Eq. 3 [33] as a function in drift and displacement ductility (**Figs. 21 (a)**).

$$\zeta = \frac{1}{4\pi}\frac{A_1}{A_2} \tag{3}$$

where A_1= energy dissipated in a cycle (the area inside the loop), and A_2= potential energy measured at the peak force of the same cycle. As shown in **Fig. 21 (a)**, column F4-24-E3(1.5)4 displayed higher energy dissipation than column F4-24-E3(0.5)4-R, the latter displaying higher ζ values until 4% drift due to the relatively higher strength of column F4-24-E3(1.5)4. However, at 6% drift, column F4-24-E3(1.5)4 reached a ζ value of 18%, which is 78% higher than column F4-24-E3(0.5)4-R.

Column F4-24-E3(0.5)4-R consistently showed higher ζ values compared to the as-built F4-24-E3(0.5)4 column indicating the successful implementation of the repair method. Between 2% to 6% drift, column F4-24-E3(0.5)4-R displayed 35% higher ζ values compared to the as-built F4-24-E3(0.5)4, reaching peak value of 17.5% at 4% drift. Beyond that, failure occurred, and both columns displayed approximately the same ζ value.

Several researchers have proposed expressions for calculating the equivalent viscous damping as a function of displacement ductility.[34] **Equations 4** [35] and **5** [36] were found to predict quite well the equivalent viscous damping of reinforced concrete columns. [34]

$$\zeta\,(\text{Gulkan and Sozen (1974)}) = 0.02 + 0.20\left(1 - \frac{1}{\sqrt{\mu}}\right) \tag{4}$$

$$\zeta\,(\text{Midorikawa et al. (2000)}) = 0.05 + 0.25\left(1 - \frac{1}{\sqrt{\mu}}\right) \tag{5}$$

Eq. 5 is similar to **Eq. 4** but with higher elastic and nonlinear damping. **Eq. 5** was able to predict ζ values quite well for column F4-24-E3(1.5)4 (**Fig. 21 (b)**) as the column behaved similarly to reinforced concrete columns in terms of yielding of the primary flexural reinforcement, i.e., steel tube. Both equations over-predicted the ζ values of F4-24-E3(0.5)4 due to the early buckling and slippage of the steel tube (**Fig. 21 (c)**). The ζ values for column F4-24-E3(0.5)4-R were slightly higher than those predicted using **Eq. 4** up to a displacement ductility of six but dropped by 40% at displacement ductility of approximately 9 due to the steel tube tearing (**Fig. 21 (d)**).

FINDINGS AND CONCLUSIONS

This paper presents an experimental investigation of the seismic behavior of three large-scale hollow-core fiber-reinforced polymer-concrete-steel (HC-FCS) columns. A HC-FCS column consisted of a concrete shell sandwiched between an outer glass fiber-reinforced polymer (GFRP) tube and an inner steel tube. Column F4-24-E3(1.5)4 had steel tube diameter-to-thickness (D_s/t_s) of 85 while columns F4-24-E3(0.5)4, and F4-24-E3(0.5)4-R had D_s/t_s of 254. Each steel tube was embedded into the footing, with an embedded length of 1.25-1.60 times its diameter, while the GFRP tube was not embedded into the footing. This study revealed the following findings and conclusions:

1- All three columns displayed displacement ductility values ranging from 5.4 to 12.0, which exceeded those required for a single column in SDC D for AASHTO guide specifications for LRFD seismic bridge design. However, the displacement ductility values for columns F4-24-E3(0.5)4 and F4-24-E3(1.5)4-R should be interpreted carefully as they occurred mainly due to steel tube slippage with limited energy dissipation. Column F4-24-E3(1.5)4 dissipated energy 230% and 330% than those of columns F4-24-E3(0.5)4-R and F4-24-E3(0.5)4, at 7.8% drift.

2- The steel tube's embedded length (L_e) is a crucial parameter for the performance of the HC-FCS columns. The embedment length, determined using Eq. 1, resulted in a high slippage of column F4-24-E3(0.5)4, while no significant slippage was observed for column F4-24-E3(1.5)4. At the peak strength of column F4-24-E3(0.5)4, the interface joint opening for column F4-24-E3(1.5)4 was 34% lower than that of column F4-24-E3(0.5)4 due to severe steel tube local buckling in the case of F4-24-E3(0.5)4.

3- There is an interaction between the concrete shell lateral dilation direction, i.e., toward the steel or GFRP tube and the relative stiffness of the GFRP and steel tubes. In the case of column F4-24-E3(0.5)4 and since the steel tube had a high D_s/t_s, concrete dilated toward the steel tube and hence displayed high slippage between the concrete shell and GFRP tube reaching 11.4 mm (0.45 in.) at a drift of 7%. However, there was no slippage between the FRP, concrete shell, and steel tubes for column F4-24-E3(1.5)4. Furthermore, this difference in the concrete dilation direction led to hoop strains of 14,700 microstrains for column F4-24-E3(1.5)4 and 4,200 microstrains for column F4-24-E3(0.5)4.

4- The accuracy of using the beam theory incorporating the confined concrete constitutive model to predict the flexural strength of the investigated columns was a function of D_s/t_s ratio. The columns displayed flexural strengths ranged from 13% to 24% lower than those calculated using the beam theory. The higher the D_s/t_s ratio is, the higher the error in the strength prediction due to the severe steel tube local buckling leading to high steel slippage and less confinement effect that occurred for high D_s/t_s.

5- The plastic hinge lengths above the footing obtained from the curvature analysis of the test data ranged from 152 mm (6.0 inches) to 165 mm (6.5 inches), which are in close agreement with the values obtained based on GFRP hoop strains criterion.

6- The implemented repair technique in the case of column F4-24-E3(0.5)4R increased the flexural strength and equivalent viscous damping by 22% and 18%, respectively, compared to those of column F4-24-E3(0.5)4.

REFERENCES

1. Schrank D, Eisele B, Lomax T, "TTI's 2012 urban mobility report," Texas A&M Transportation Institute The Texas A&M University System. 2012, pp. 4.

2. Schrank DL, Lomax TJ, "2009 urban mobility report." Texas Transportation Institute, Texas A & M University; 2009.

3. Dawood H, ElGawady M, Hewes J, "Factors affecting the seismic behavior of segmental precast bridge columns," Frontiers of Structural and Civil Engineering, V. 8, No. 4. 2014, pp. 388-98.

4. Lin M, Tsai K-C, "Behavior of double-skinned composite steel tubular columns subjected to combined axial and flexural loads," In Proc. of the First International Conference on the Steel & Composite Structures, pp. 1145-1152. 2001

5. Tao Z, Han L-H, "Behaviour of concrete-filled double skin rectangular steel tubular beam–columns," Journal of Constructional Steel Research, V. 62, No. 7. 2006, pp. 631-46.

6. Wei S, Mau S, Vipulanandan C, Mantrala S, "Performance of new sandwich tube under axial loading: experiment," Journal of structural engineering, V. 121, No. 12. 1995, pp. 1806-14.

7. Zhao X-L, Han B, Grzebieta RH, "Plastic mechanism analysis of concrete-filled double-skin (SHS inner and SHS outer) stub columns," Thin-Walled Structures, V. 40, No. 10. 2002, pp. 815-33.

8. Anumolu S, Abdelkarim OI, ElGawady MA, "Behavior of Hollow-Core Steel-Concrete-Steel Columns Subjected to Torsion Loading," Journal of Bridge Engineering. 2016, pp. 04016070.

9. Teng J, Lam L, "Behavior and modeling of fiber reinforced polymer-confined concrete," Journal of structural engineering, V. 130, No. 11. 2004, pp. 1713-23.

10. Teng J, Yu T, Wong Y, Dong S, "Hybrid FRP–concrete–steel tubular columns: concept and behavior," Construction and Building Materials, V. 21, No. 4. 2007, pp. 846-54.

11. Wong Y, Yu T, Teng J, Dong S, "Behavior of FRP-confined concrete in annular section columns," Composites Part B: Engineering, V. 39, No. 3. 2008, pp. 451-66.

12. Abdulazeez MM, Gheni A, Abdelkarim OI, ElGawady MA, "Column-Footing Connection Evaluation of Hollow-Core Composite Bridge Columns," Special Publication, V. 327. 2018, pp. 39.1-.14.

13. Abdelkarim OI, ElGawady MA, Gheni A, Anumolu S, Abdulazeez M, "Seismic Performance of Innovative Hollow-Core FRP–Concrete–Steel Bridge Columns," Journal of Bridge Engineering. 2016, pp. 04016120.

14. Yu T, Wong Y, Teng J, "Technical Papers: Behavior of hybrid frp-concrete-steel double-skin tubular columns subjected to eccentric compression," Advances in Structural Engineering, V. 13, No. 5. 2010, pp. 961-74.

15. Issa CA, Debs P, "Experimental study of epoxy repairing of cracks in concrete," Construction and Building Materials, V. 21, No. 1. 2007, pp. 157-63.

16. Karayannis CG, Sirkelis GM, "Strengthening and rehabilitation of RC beam–column joints using carbon-FRP jacketing and epoxy resin injection," Earthquake Engineering & Structural Dynamics, V. 37, No. 5. 2008, pp. 769-90.

17. Saini A, Saiidi MS, "Post-earthquake damage repair of various reinforced concrete bridge components," Caltrans Final Rep CA, V. 142179. 2013.

18. Fakharifar M, Chen G, Arezoumandi M, ElGawady M, "Hybrid jacketing for rapid repair of seismically damaged reinforced concrete columns," Transportation Research Record: Journal of the Transportation Research Board, No. 2522. 2015, pp. 70-8.

19. Abdulazeez MM, Gheni A, Colbert N, ElGawady MA, "Seismic Performance and Retrofit Evaluation of Hollow-Core Composite Bridge Columns," Maintenance, Safety, Risk, Management and Life-Cycle Performance of Bridges, CRC Press, 2018, pp. 437-44.

20. Abdelkarim OI, ElGawady MA, "Analytical and finite-element modeling of FRP-concrete-steel double-skin tubular columns," Journal of Bridge Engineering, V. 20, No. 8. 2015, pp. B4014005.

21. Yu T, Wong Y, Teng J, Dong S, "Structural behavior of hybrid FRP-concrete-steel double-skin tubular columns," Vol. 68, no. 05. 2007.

22. Abdelkarim OI, ElGawady MA, Anumolu S, Gheni A, Sanders GE, "Behavior of hollow-core FRP-concrete-steel columns under static cyclic flexural loading," Journal of Structural Engineering, V. 144, No. 2. 2017, pp. 04017188.

23. Anumolu S, Abdelkarim OI, Abdulazeez MM, Gheni A, ElGawady MA, "Hollow-Core FRP–Concrete–Steel Bridge Columns under Torsional Loading," Fibers, V. 5, No. 4. 2017, pp. 44.

24. American Welding Society (AWS). Structural Welding Committee, American National Standards Institute, and AWS. Technical Activities Committee. "*Structural welding code--seismic supplement*. *Supersedes AWS D1.8/D1.8M:2005* " Amer Welding Society, 2006.

25. du Beton, Federation Internationale. "Seismic bridge design and retrofit—structural solutions." *fib Bulletin* 39 (2007).

26. FEMA A, "461/Interim Testing Protocols for Determining the Seismic Performance Characteristics of Structural and Nonstructural Components," Applied Technology Council, Redwood City, CA. 2007, pp. 113.

27. Yu T, Wong Y, Teng J, Dong S, Lam E, "Flexural behavior of hybrid FRP-concrete-steel double-skin tubular members," Journal of Composites for Construction, V. 10, No. 5. 2006, pp. 443-52.

28. Fakharifar M, Chen G, Wu C, Shamsabadi A, ElGawady MA, Dalvand A, "Rapid repair of earthquake-damaged RC columns with prestressed steel jackets," Journal of Bridge Engineering, V. 21, No. 4. 2016, pp. 04015075.

29. Miranda E, Bertero VV, "Evaluation of strength reduction factors for earthquake-resistant design," Earthquake spectra, V. 10, No. 2. 1994, pp. 357-79.

30. Transportation Officials Subcommittee on Bridges, "AASHTO guide specifications for LRFD seismic bridge design." AASHTO; 2011.

31. Sullivan T, Calvi G, Priestley M, "Initial stiffness versus secant stiffness in displacement based design," In 13th World Conference of Earthquake Engineering (WCEE), no. 2888. 2004

32. Youssf O, ElGawady MA, Mills JE, "Displacement and plastic hinge length of FRP-confined circular reinforced concrete columns," Engineering Structures, V. 101. 2015, pp. 465-76.

33. Calvi G, Priestley M, Kowalsky M, "Displacement-based seismic design of structures," In New Zealand Conference on Earthquake Engineering, 2007, p. 740. IUSS press, 2007.

34. ElGawady M, Endeshaw M, McLean D, Sack R, "Retrofitting of rectangular columns with deficient lap splices," Journal of Composites for Construction, V. 14, No. 1. 2009, pp. 22-35.

35. Gulkan P, Sozen MA, "Inelastic responses of reinforced concrete structures to earthquake motions," Special Publication, V. 53. 1977, pp. 109-16.

36. Midorikawa M, Hiraishi H, Okawa I, Iiba M, Teshigawara M, Isoda H, "Development of seismic performance evaluation procedures in building code of Japan," In Proceedings of 12th World Conference of Earthquake Engineering, Auckland, Paper, no. 2215. 2000.

List of symbols:

D_s/t_s	Steel tube diameter-to-thickness ratio
D_f	FRP tube diameter
L_e	Steel tube’s embedded length
H/D_f	The column shear span-to-depth ratio (=M/VD)
f_u	The ultimate stress of the steel tube
$f'_{c,F}$	The unconfined cylindrical compressive strength of the concrete footing
P_o	The axial load capacity of an equivalent RC-column
δ_y	First yield column displacement
δ_u	Displacement at the maximum moment capacity
δ_f	Ultimate column displacement
ϕ	Column curvature
Δ_1 and Δ_2	Vertical displacements at the sides of the investigated column
D	The horizontal separation distance between the two potentiometers used for measuring the vertical displacements
L	The vertical gauge length of the potentiometers
δ_{iy}	Idealized yield displacement
δ_f	Ultimate displacement at failure
μ	Displacement ductility
K_i	Initial idealized stiffness
F_{iy}	Idealized lateral force correspondent to δ_{iy}
K_{sec}	Secant stiffness normalized by the yield stiffness
$\varepsilon_b/\varepsilon_y$	Steel tube buckling-to-yield strain

δ_r / δ_b	Steel tube first buckling-to-the ultimate drift
L_p	Plastic hinge length of a CFFT column where the hoop strain value on the GFRP drops to one-third of its peak value
JO	HC-FCS column joint opening
ζ	Equivalent viscous damping
A_1	The energy dissipated in a cycle (the area inside the loop)
A_2	Potential energy measured at the peak force of the same cycle

TABLES AND FIGURES

List of Tables:

List of Figures:

Fig. 9 – Curvature along the height of the tested HC-FCS columns (a) F4-24-E3(1.5)4, (b) F4-24-E3(0.5)4, and (c) F4-24-E3(0.5)4-R.

Fig. 10 – Steel tube strain-drift hysteresis at the interface joint (a) F4-24-E3(1.5)4 vertical -north, (b) F4-24-E3(1.5)4 horizontal- south, (c) F4-24-E3(0.5)4 south-vertical, and (d) F4-24-E3(0.5)4 north-horizontal.

Fig. 11 – F4-24-E3(1.5)4 column (a) inward local buckling (south side), (b) tearing (north side) at 8.0% drift, (c) concrete shell crushing at the interface joint, and (d) undamaged footing.

Fig. 12 – F4-24-E3(0.5)4 column steel tube inward local buckling (a) from outside at 5.8% drift, and (b) from inside (north-west side) at 7.5% drift.

Fig. 13 – F4-24-E3(0.5)4-R column (a) steel tube inward buckling and tearing at the interface joint at 6% drift, (b) close-up view, and (c) undamaged footing.

Fig. 14 – Experimental versus analytical stiffness degradations.

Fig. 15 – HC-FCS column steel tube (a) (buckling / yield) strain versus D_s/t_s ratios, and (b) (rupture/ buckling) displacement versus D_s/t_s ratios.

Fig. 16 – FRP strain profiles at different drift levels (a) F4-24-E3(1.5)4, (b) F4-24-E3(1.5)4, (c) F4-24-E3(1.5)4, (d) F4-24-E3(1.5)4, (e) F4-24-E3(0.5)4, and (f) three tested columns (horizontal direction) at 6% drift.

Fig. 17 –GFRP tube strain-drift hysteresis at the interface joint (a) F4-24-E3(1.5)4 (vertical -north side), (b) F4-24-E3(1.5)4 (horizontal- north side),(c) F4-24-E3(0.5)4 (vertical -south side), (d) F4-24-E3(0.5)4 (horizontal- south side), (e) F4-24-E3(0.5)4-R (vertical -south side), and (f) horizontal- south side.

Fig. 18 – Plastic hinge length (a) F4-24-E3(1.5)4 (horizontal strain profile), (b) F4-24-E3(1.5)4 (curvature along the height-closer view), (c) F4-24-E3(0.5)4 (horizontal strain profile), and (d) F4-24-E3(0.5)4 (curvature along the height-closer view).

Fig. 19 – Relative movements of the FRP tube, concrete shell, and inner steel tube measured vs. drift (%) for HC-FCS column (a) F4-24-E3(1.5)4, (b) F4-24-E3(0.5)4, and (c) the tested HC-FCS columns.

Fig. 20 – Cumulative energy dissipation vs. drift for the tested HC-FCS columns.

Fig. 21 – Equivalent viscous damping vs. displacement ductility for the tested HC-FCS columns (a) equivalent viscous damping vs. drift, (b) F4-24-E3(1.5)4, (c) F4-24-E3(0.5), and (d) F4-24-E3(0.5)4-R.

Table 1 – Characteristics of the used steel tubes

Column name	Thickness, (t_s) mm (inch)	D_s/t_s	Embedded length, (L_e) mm (inch)	L_e/D_s	TR* ($=t_s/t_f$)	Yield stress, MPa (ksi)	Ultimate stress, MPa (ksi)	Ultimate strain, (ε_u, in/in)
F4-24-E3(1.5)4	4.8 (0.188)	85	635 (25)	1.60	0.50	399 (58)	441 (64)	0.21
F4-24-E3(0.5)4	1.6 (0.063)	254	508 (20)	1.25	0.17	355 (51)	368 (53)	0.24

**TR: Inner-to-outer tubes (Steel to FRP tubes) thicknesses ratio*

Table 2 – GFRP tubes properties based on the manufacturer's reported data

FRP type	Elastic modulus, GPa (10^3 ksi)	Hoop elastic Modulus, GPa (10^3 ksi)	Axial tensile ultimate stress, MPa (ksi)	Hoop rupture stress, MPa (ksi)
E-GFRP	4.7 (0.68)	21 (3.02)	65.7 (9.53)	276.8 (40.1)

Table 3 – Mixture used for the concrete shells

w/c	Cement, kg/m^3 (lb/yd^3)	Fly Ash, kg/m^3 (lb/yd^3)	Water, kg/m^3 (lb/yd^3)	Fine aggregate, kg/m^3 (lb/yd^3)	Coarse aggregate,* kg/m^3 (lb/yd^3)	HRWR,** kg/m^3 (lb/yd^3)
0.5	590 (350)	170 (101)	380 (225)	1430 (848)	1430 (848)	3.2 (1.9)

* Pea gravel with a maximum aggregate size of 9.5 mm (0.375 inches).
** *High range water reducer.*

Table 4 – Unconfined concrete strength

	F4-24-E3(1.5)4		F4-24-E3(0.5)4	
	Column	Footing	Column	Footing
f'_c at 28 days, MPa (ksi)	35.0 (5.3)	55 (8)	43.5 (6.3)	37.5 (5.4)
f'_c day of test, MPa (ksi)	46.5 (6.8)	56.7 (8.2)	46.3 (6.7)	41.6 (6.0)

Table 5–Concrete infill mixture proportions and strength

w/c	Cement-III, kg/m^3 (lb/yd^3)	Water, kg/m^3 (lb/yd^3)	Fine aggregate, kg/m^3 (lb/yd^3)	Coarse aggregate, kg/m^3 (lb/yd^3)	HRWR, kg/m^3 (lb/yd^3)	Unconfined concrete strength (f'_c)*, MPa (psi)
0.5	451 (760)	225 (380)	932 (1,570)	554 (933)	1.2 (2)	35.7 (5.18)

* At the day of the test

Table 6 – Results of the investigated columns

Tested column	M_{max} kN.m (kips.ft)	δ_{iy}, mm (inch)	δ_u, mm (inch)	δ_f, mm (inch)	K_i	Mode of failure
F4-24-E3(1.5)4	713 (526)	32 (1.5)	69.5 (2.70)	204 (8.10)	42.7	Steel tube local buckling, concrete shell crushing, and steel tube tearing
F4-24-E3(0.5)4	312 (230)	17.8 (0.65)	39 (1.87)	198 (7.80)	41.5	Steel tube severe local buckling, concrete shell crushing
F4-24-E3(0.5)4-R	339 (250)	14 (0.65)	101.6 (4.00)	195.6 (6.00)	46.9	Steel tube tearing, concrete infill crushing

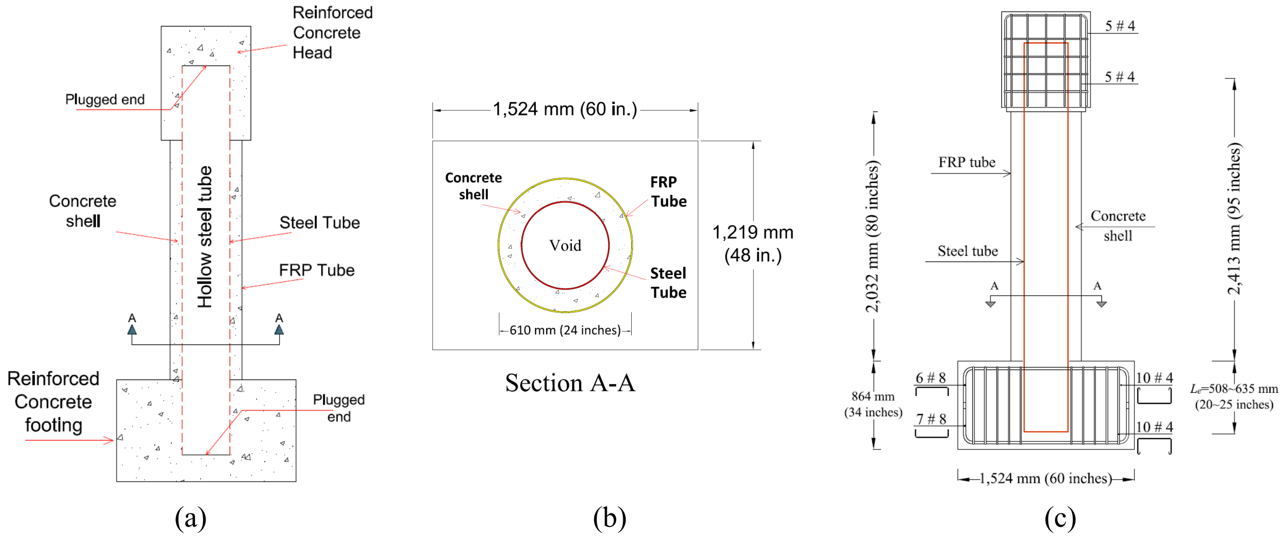

Fig. 1 – HC-FCS column (a) general assembly, (b) cross section, and (c) layout

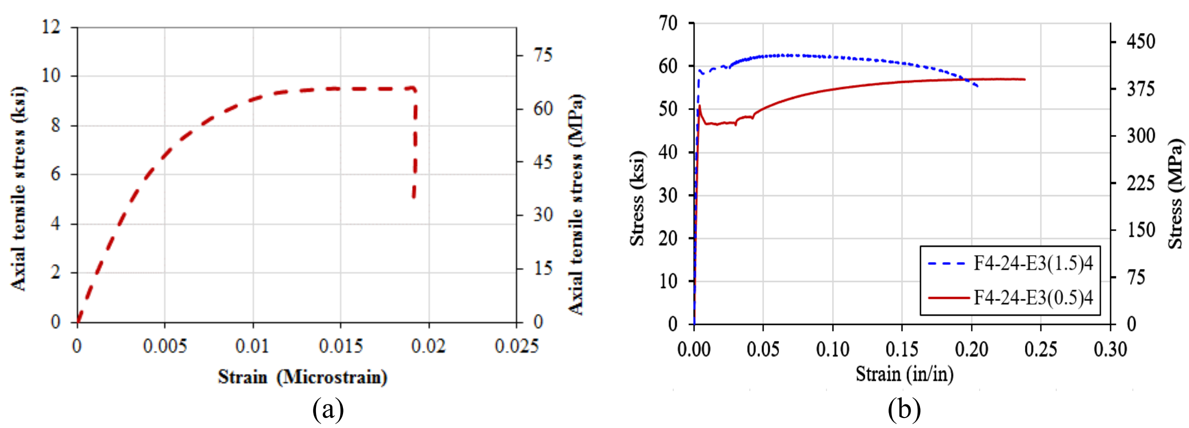

Fig. 2 – Average stress-strain curve (a) GFRP coupon, and (b) steel coupons

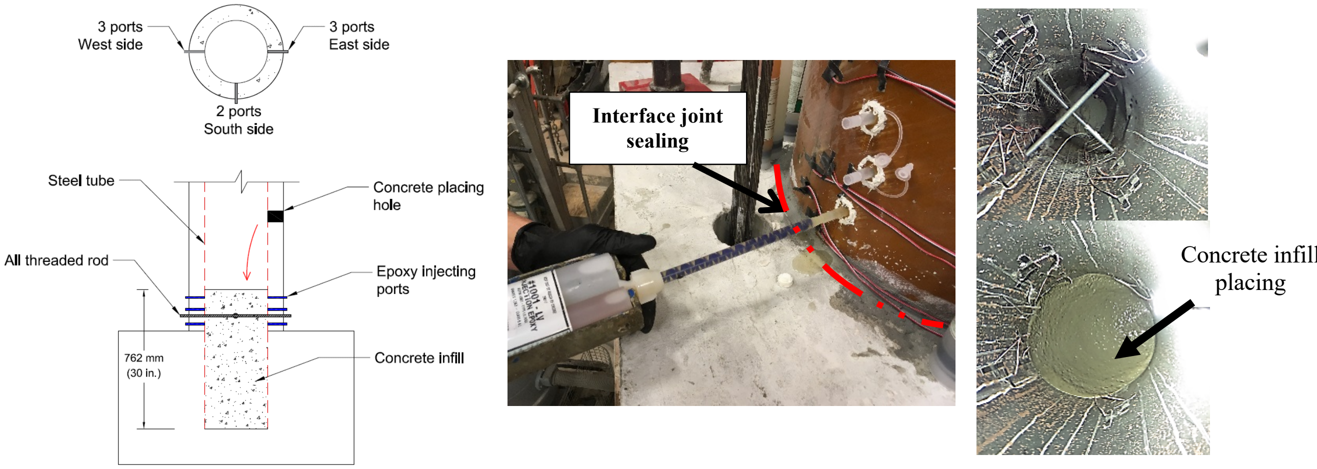

(a) (b) (c)

Fig. 3 – Steel tube concrete infill procedure (a) layout, (b) injecting the epoxy, and (c) all thread rods and concrete infill placing

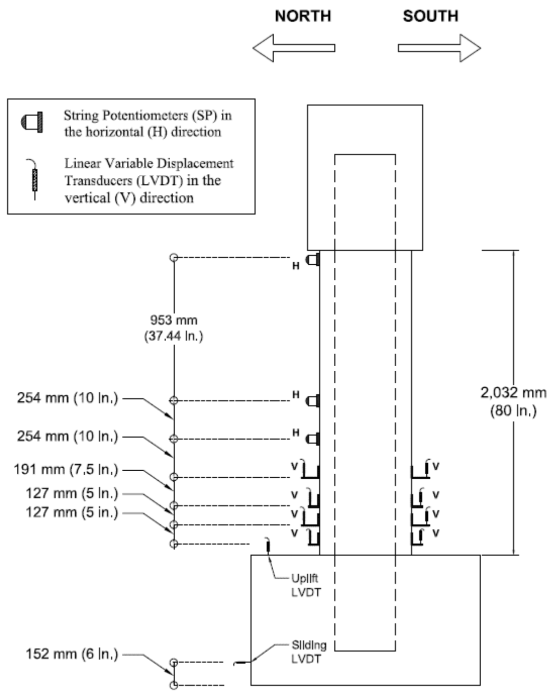

(a)

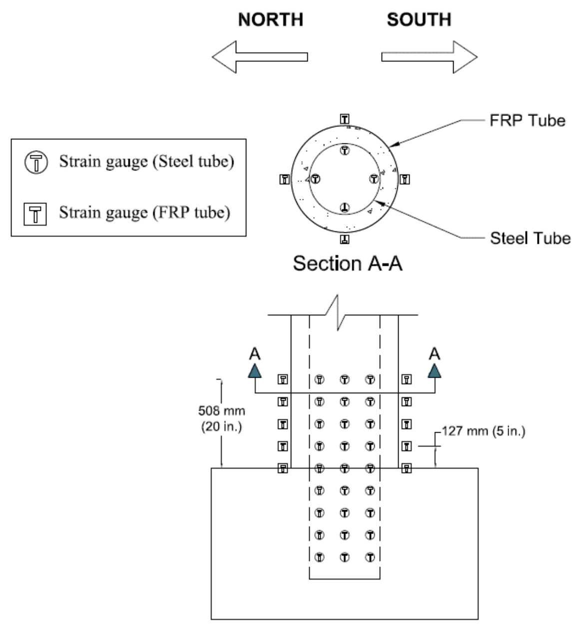

(b)

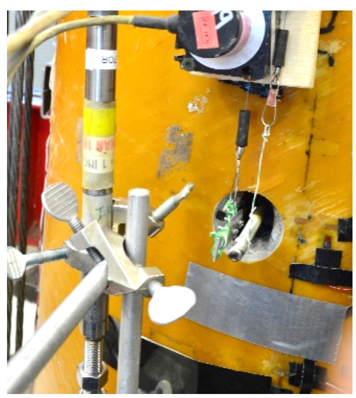

(c)

Fig. 4 – Instrumentation (a) LVDTs and SPs layout, (b) strain gauges' layout, and (c) relative movement SP measurement

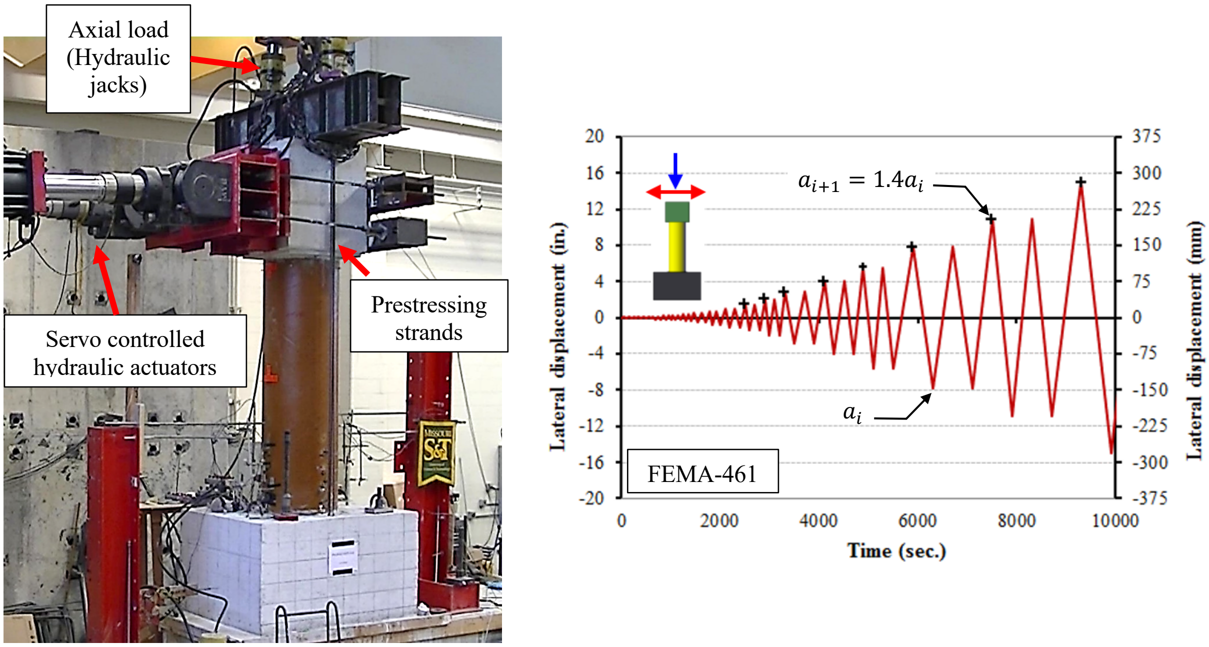

(a) (b)

Fig. 5 – Column testing: (a) a column ready for testing, and (b) lateral displacement loading regime

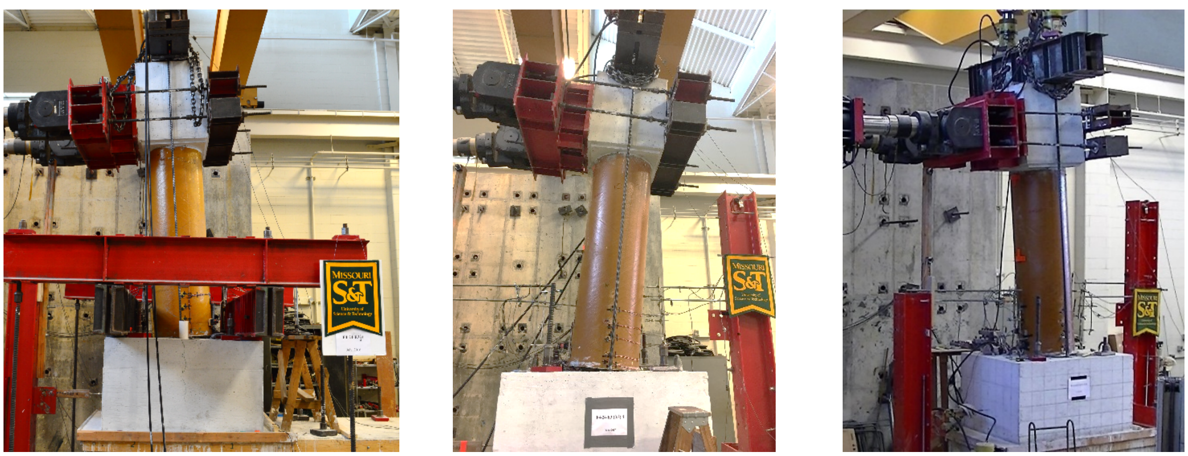

(a) (b) (c)

Fig. 6 – HC-FCS columns at the test (a) F4-24-E3(1.5)4, (b) F4-24-E3(0.5)4, and (c) F4-24-E3(0.5)4-R.

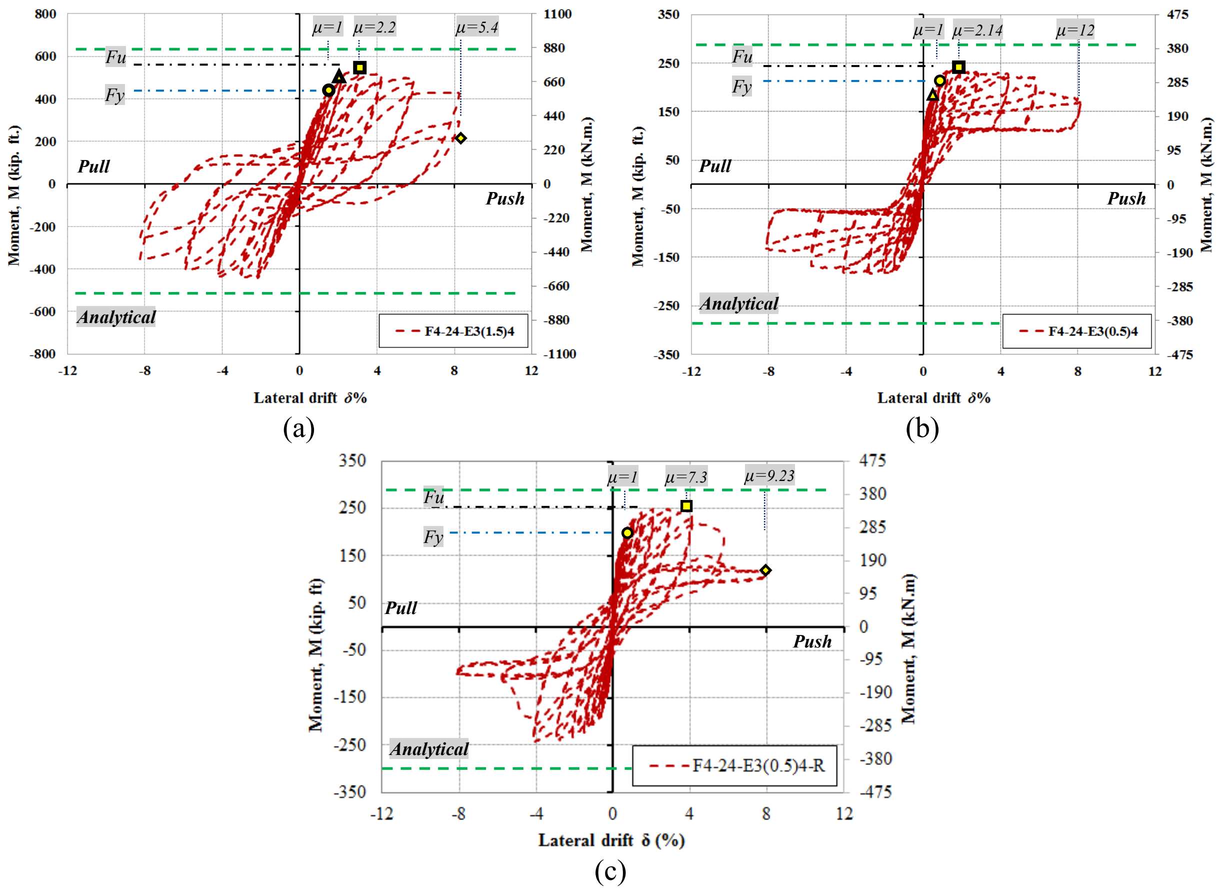

○ *Steel tube yielding* ∆ *Steel tube buckling* ◊ *Steel tube tearing* □ *Ultimate strength*

Fig. 7 – Moment-drift relation of the tested HC-FCS columns (a) F4-24-E3(1.5)4, (b) F4-24-E3(0.5)4, and (c) F4-24-E3(0.5)4-R

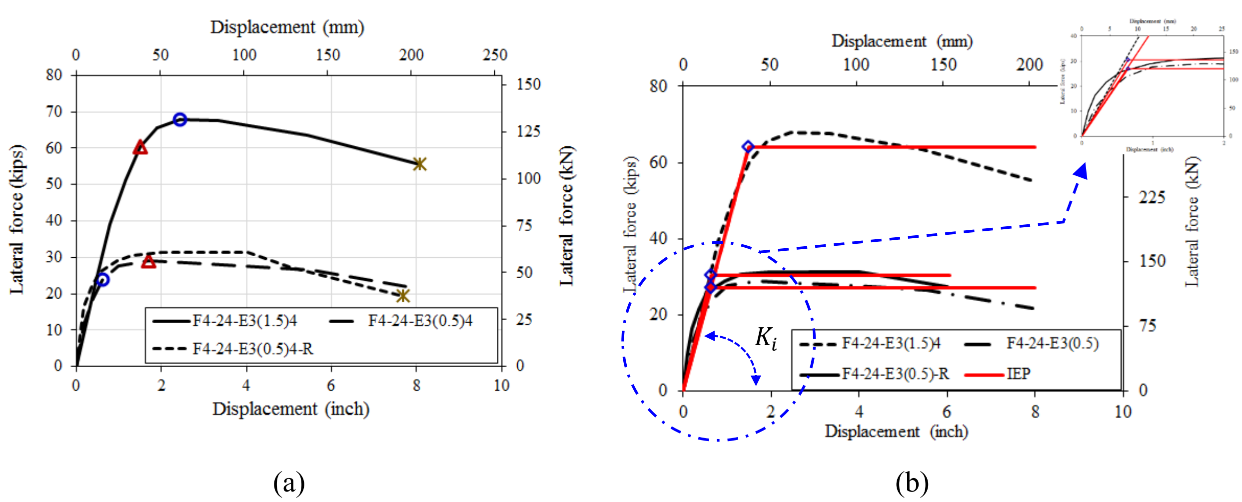

∆ *Steel tube yielding* ○ *Steel tube buckling* ∗ *Steel tube tearing*

Fig. 8 – Backbone curves for the tested HC-FCS columns (a) experimental, and (b) idealized elasto-plastic curve

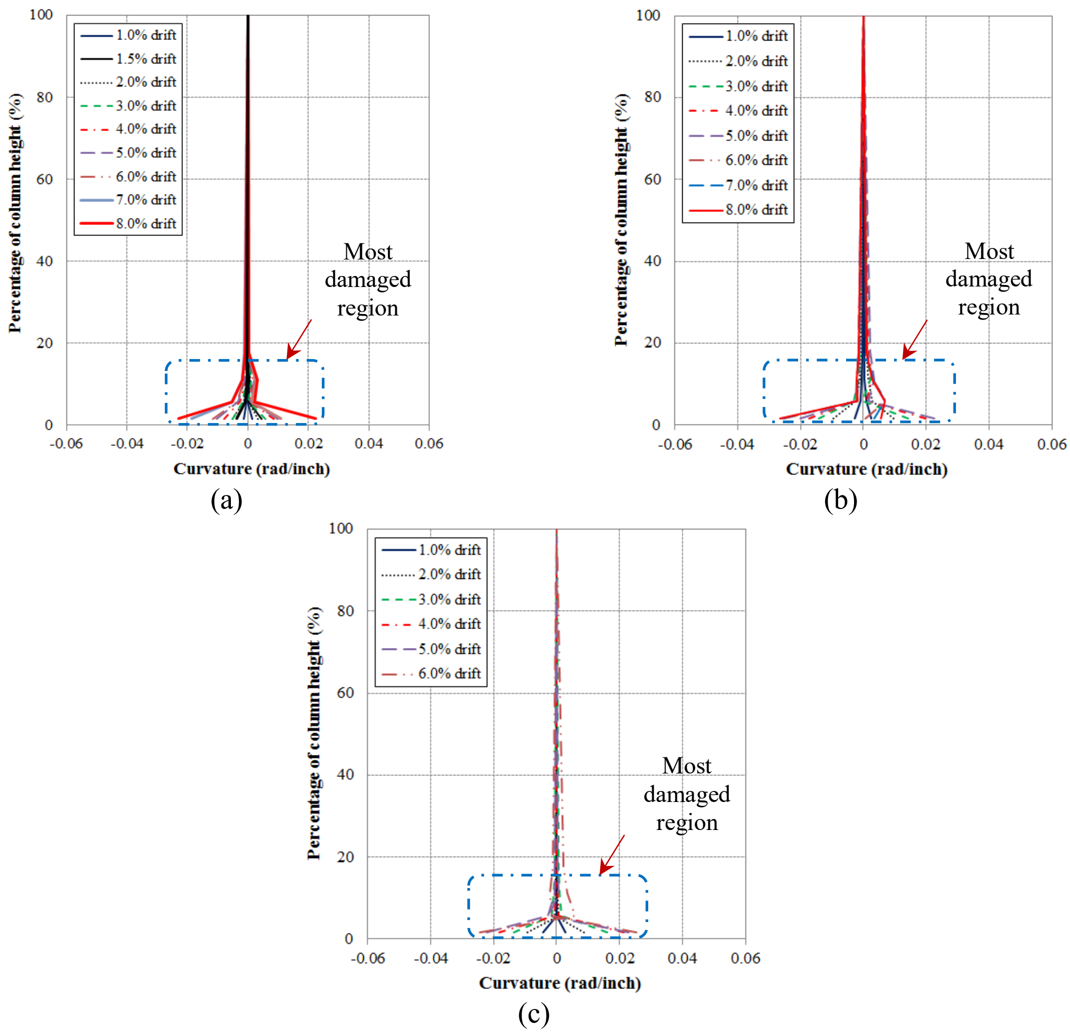

Fig. 9 – Curvature along the height of the tested HC-FCS columns (a) F4-24-E3(1.5)4, (b) F4-24-E3(0.5)4, and (c) F4-24-E3(0.5)4-R

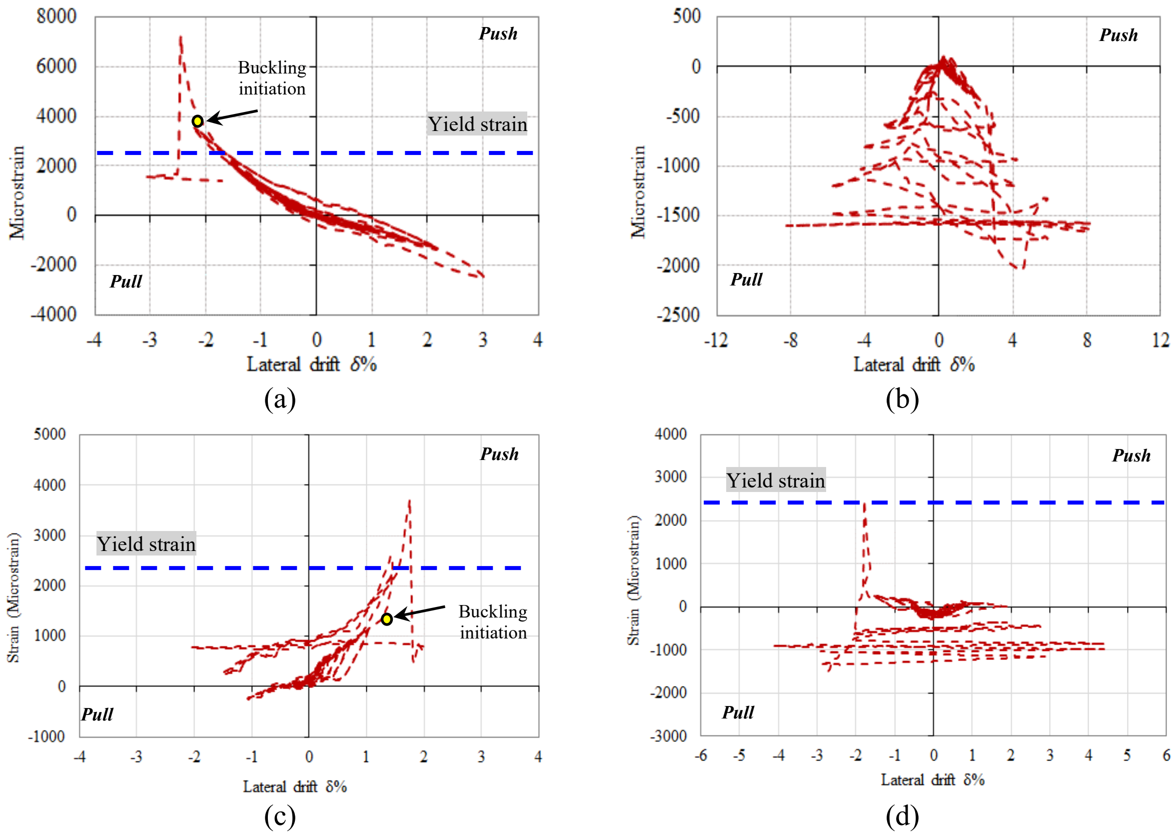

Fig. 10 – Steel tube strain-drift hysteresis at the interface joint (a) F4-24-E3(1.5)4 vertical - north, (b) F4-24-E3(1.5)4 horizontal- south, (c) F4-24-E3(0.5)4 south-vertical, and (d) F4-24-E3(0.5)4 north-horizontal

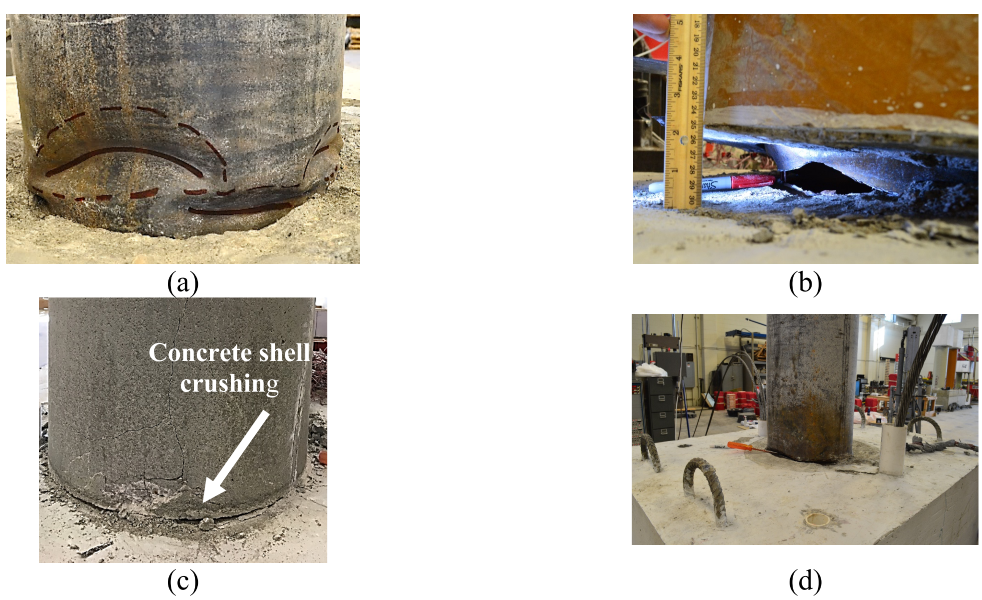

Fig. 11 – F4-24-E3(1.5)4 column (a) inward local buckling (south side), (b) tearing (north side) at 8.0% drift, (c) concrete shell crushing at the interface joint, and (d) undamaged footing

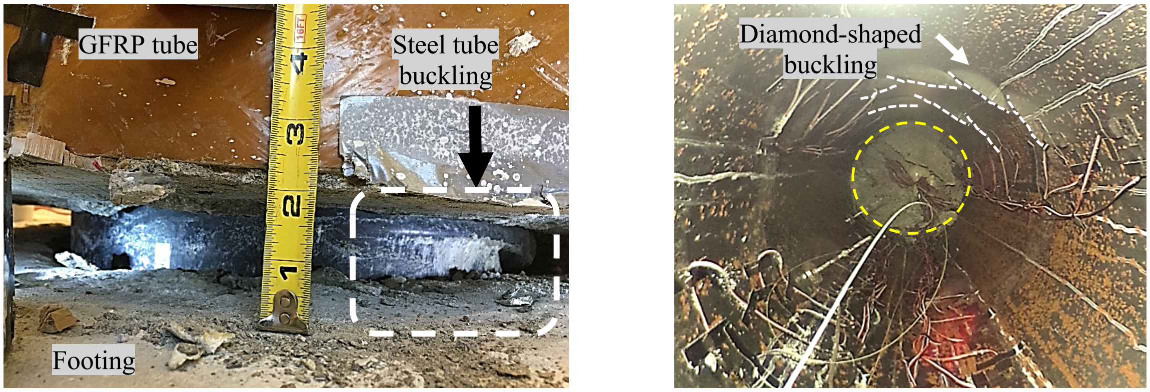

(a) (b)

Fig. 12 – F4-24-E3(0.5)4 column steel tube inward local buckling (a) from outside at 5.8% drift, and (b) from inside (north-west side) at 7.5% drift

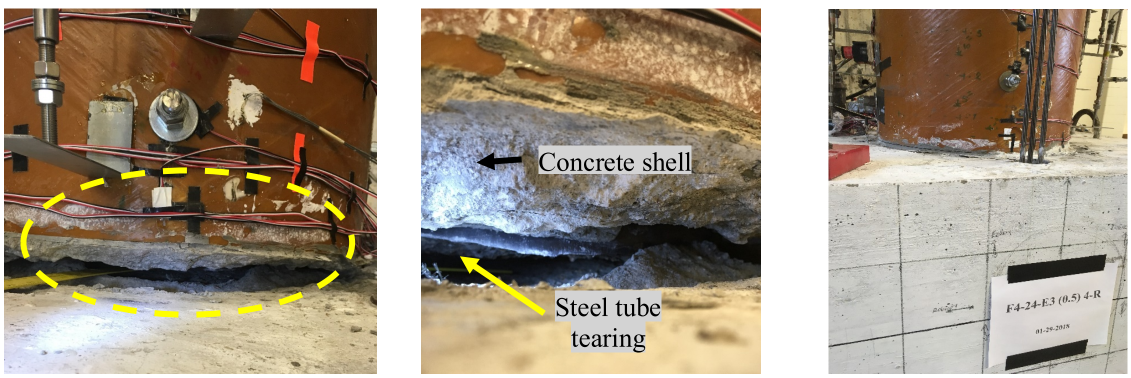

(a) (b) (c)

Fig. 13 – F4-24-E3(0.5)4-R column (a) steel tube inward buckling and tearing at the interface joint at 6% drift, (b) close-up view, and (c) undamaged footing

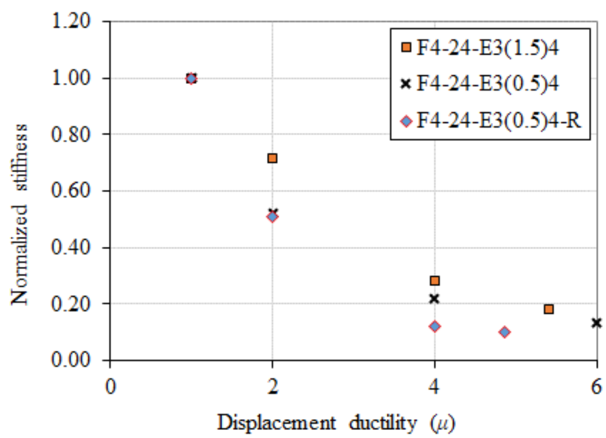

Fig. 14 – Experimental versus analytical stiffness degradations

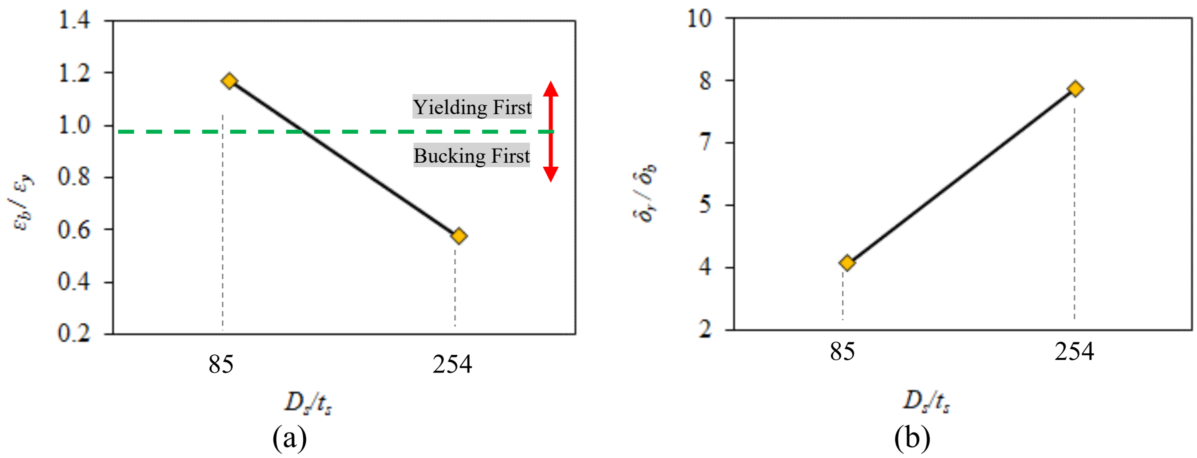

Fig. 15 – HC-FCS column steel tube (a) buckling-to-yield strain versus D_s/t_s ratios, and (b) rupture-to-buckling displacement versus D_s/t_s ratios

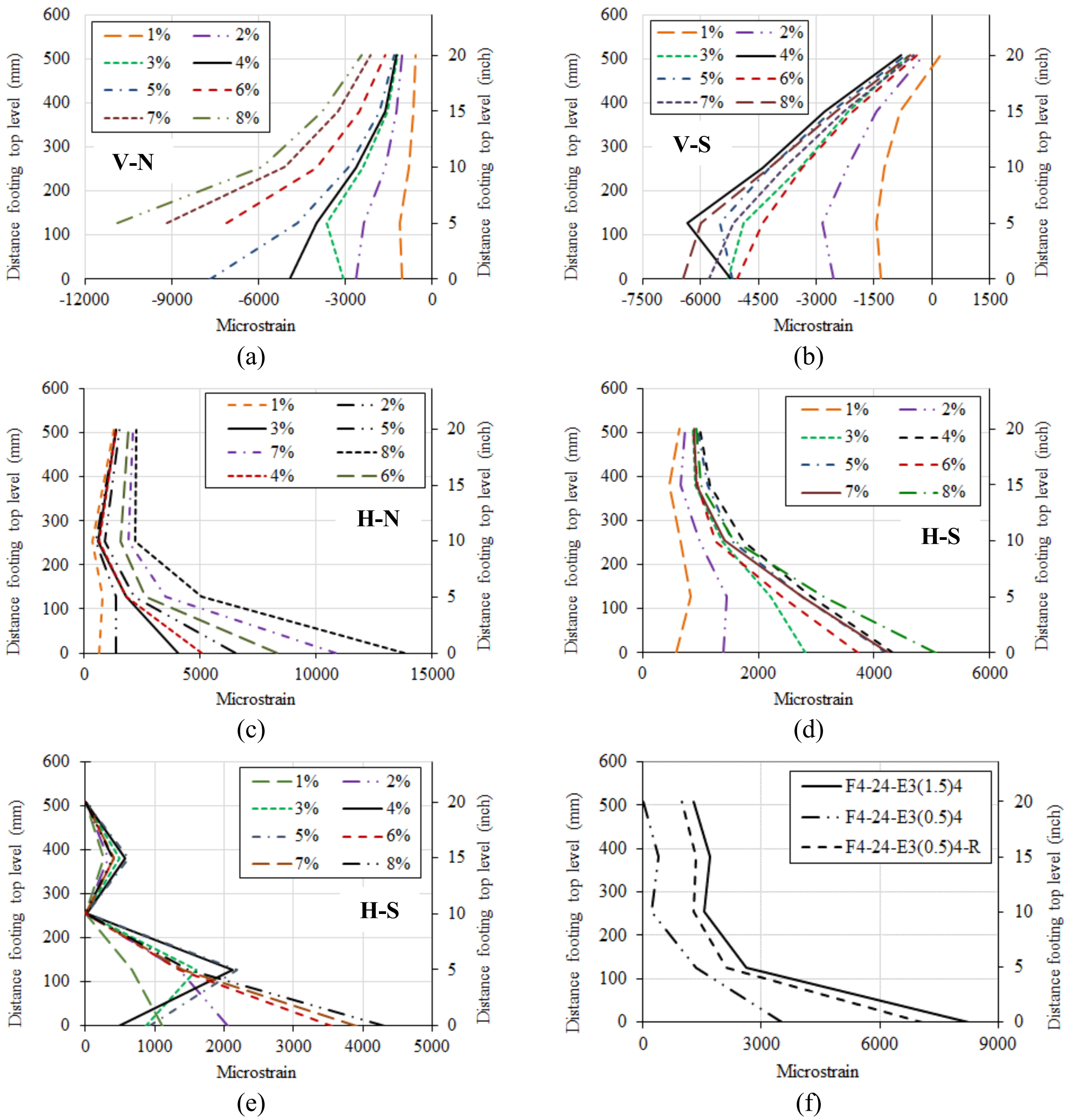

V: vertical H:horizontal S:south N:North

Fig. 16 – FRP strain profiles at different drift levels (a) F4-24-E3(1.5)4, (b) F4-24-E3(1.5)4, (c) F4-24-E3(1.5)4, (d) F4-24-E3(1.5)4, (e) F4-24-E3(0.5)4, and (f) three tested columns (horizontal direction) at 6% drift

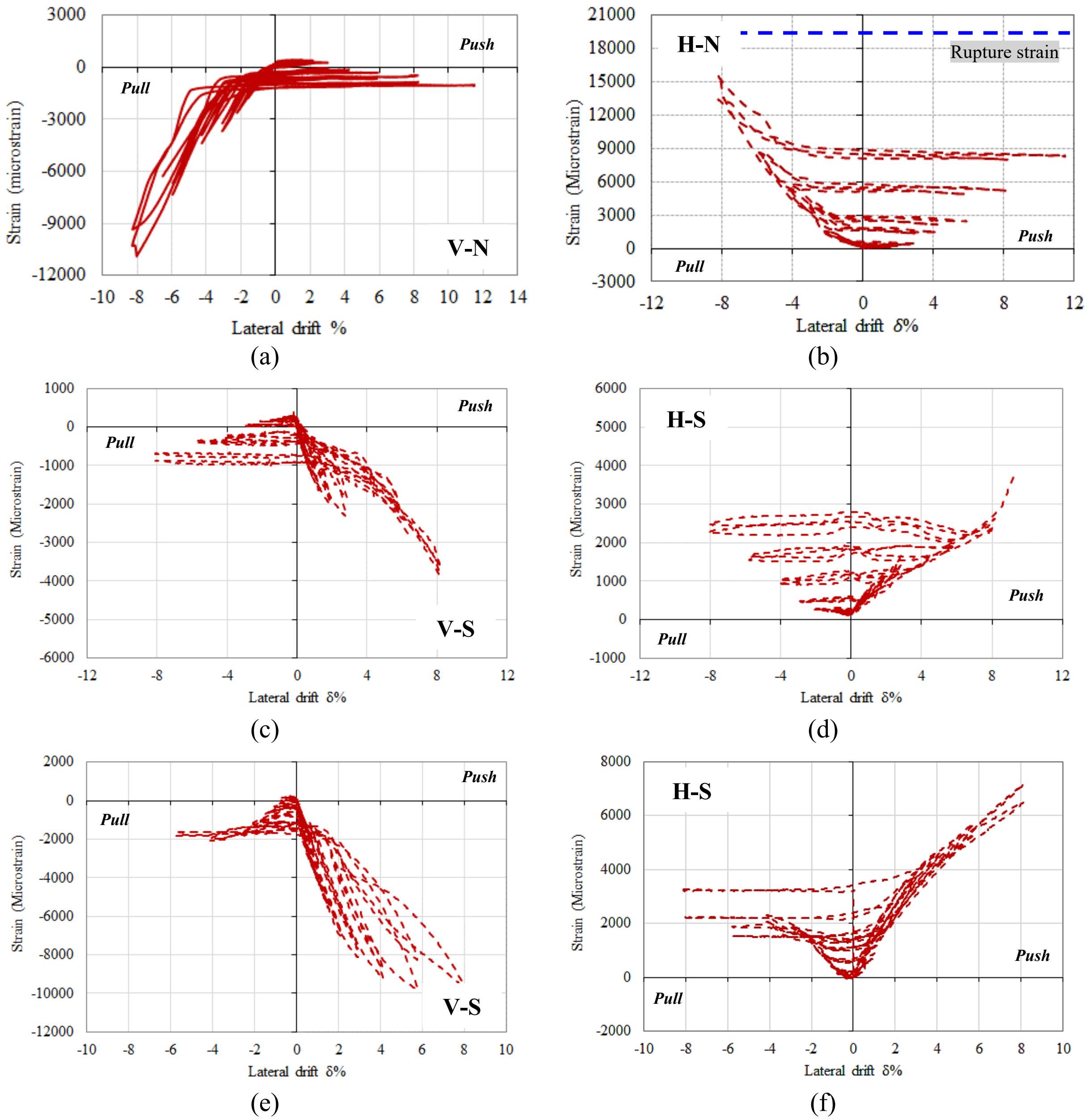

V: vertical H:horizontal S:south N:North

Fig. 17 –GFRP tube strain-drift hysteresis at the interface joint (a) F4-24-E3(1.5)4 (vertical - north side), (b) F4-24-E3(1.5)4 (horizontal- north side),(c) F4-24-E3(0.5)4 (vertical -south side), (d) F4-24-E3(0.5)4 (horizontal- south side), (e) F4-24-E3(0.5)4-R (vertical -south side), and (f) horizontal- south side

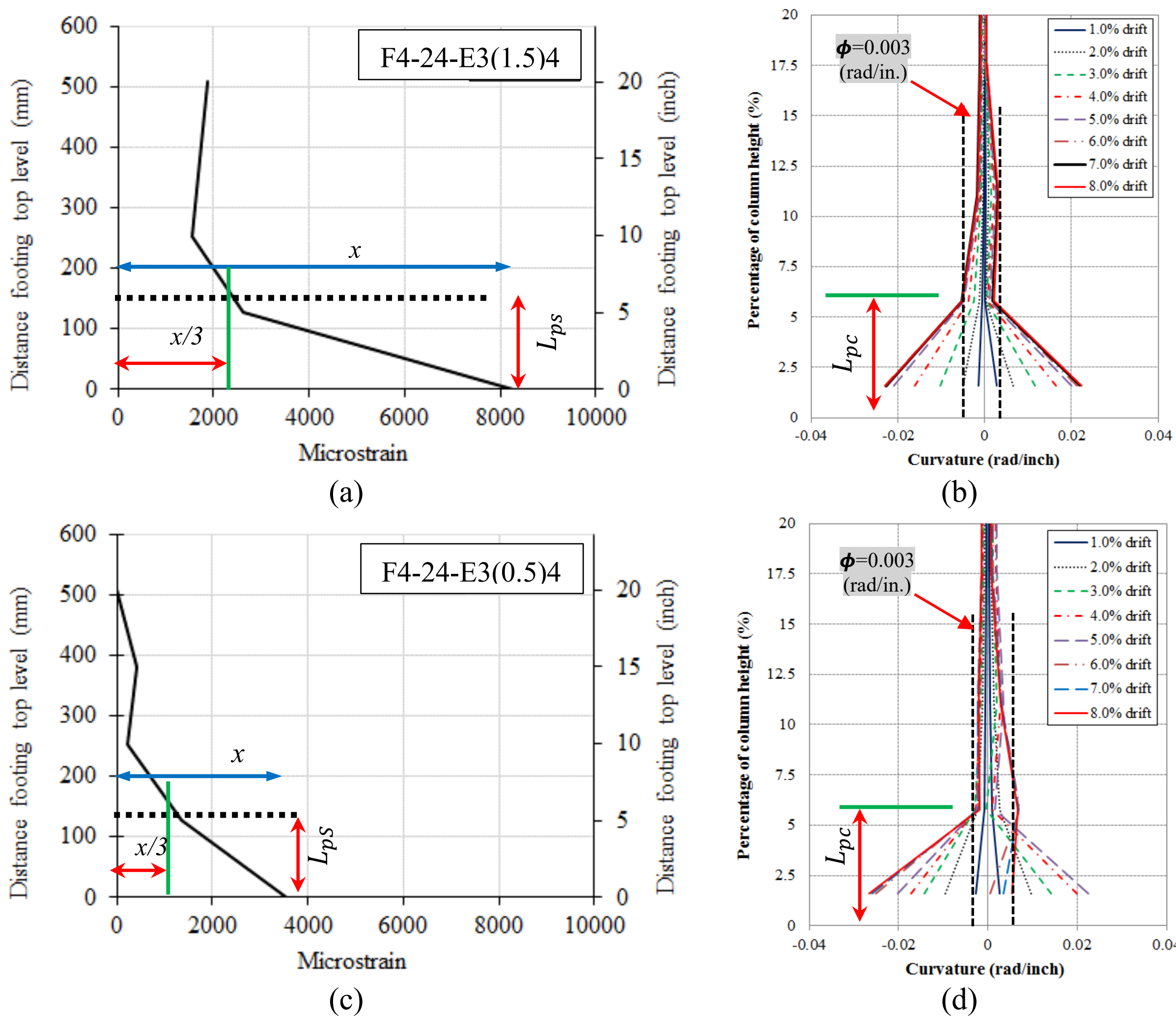

Fig. 18 – Plastic hinge length (a) F4-24-E3(1.5)4 (horizontal strain profile), (b) F4-24-E3(1.5)4 (curvature along the height-closer view), (c) F4-24-E3(0.5)4 (horizontal strain profile), and (d) F4-24-E3(0.5)4 (curvature along the height-closer view)

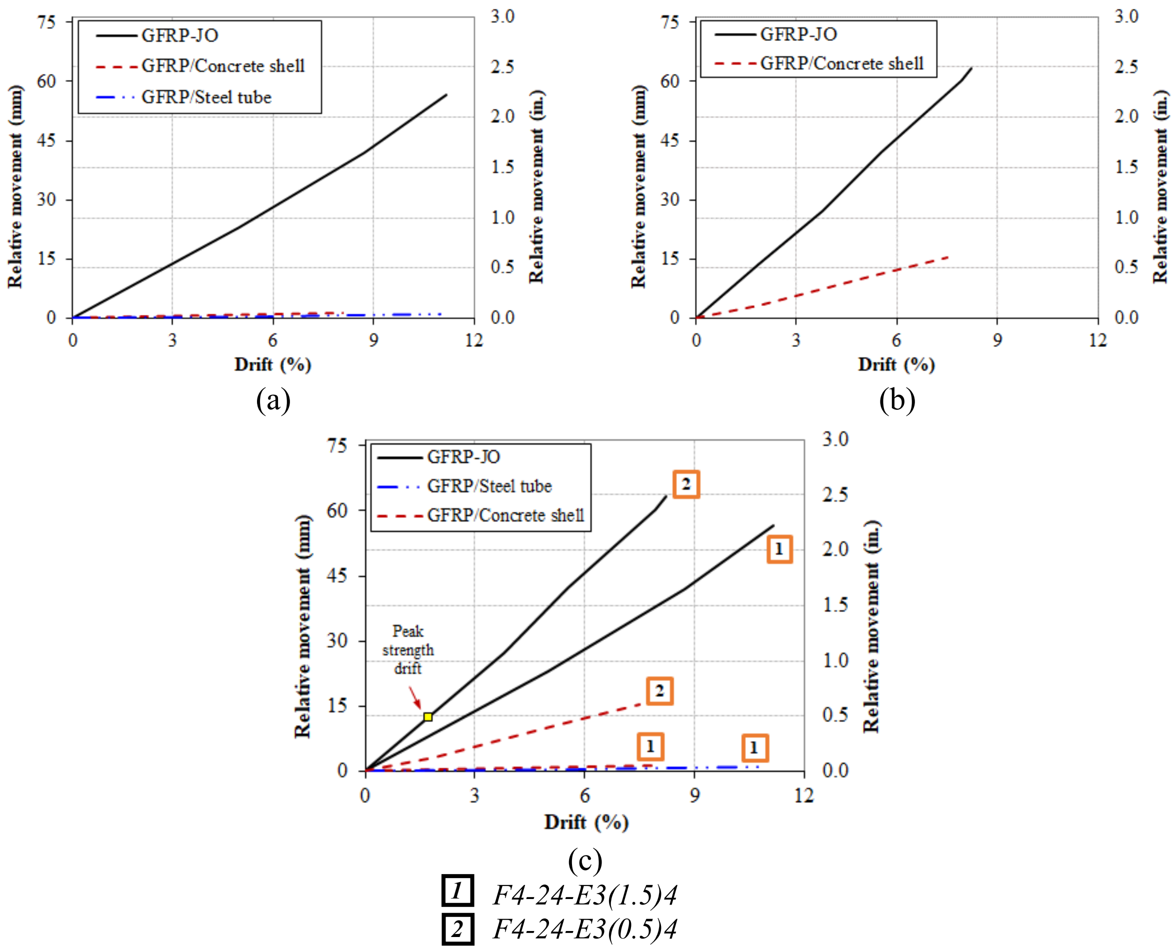

Fig. 19 – Relative movements of the FRP tube, concrete shell, and inner steel tube measured vs. drift (%) for HC-FCS column (a) F4-24-E3(1.5)4, (b) F4-24-E3(0.5)4, and (c) the tested HC-FCS columns

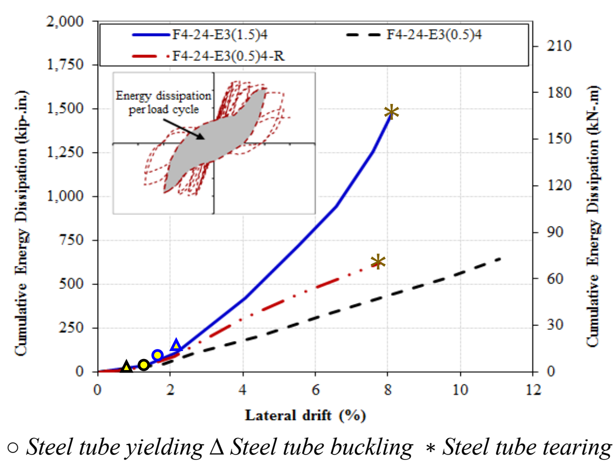

Fig. 20 – Cumulative energy dissipation vs. drift for the tested HC-FCS columns

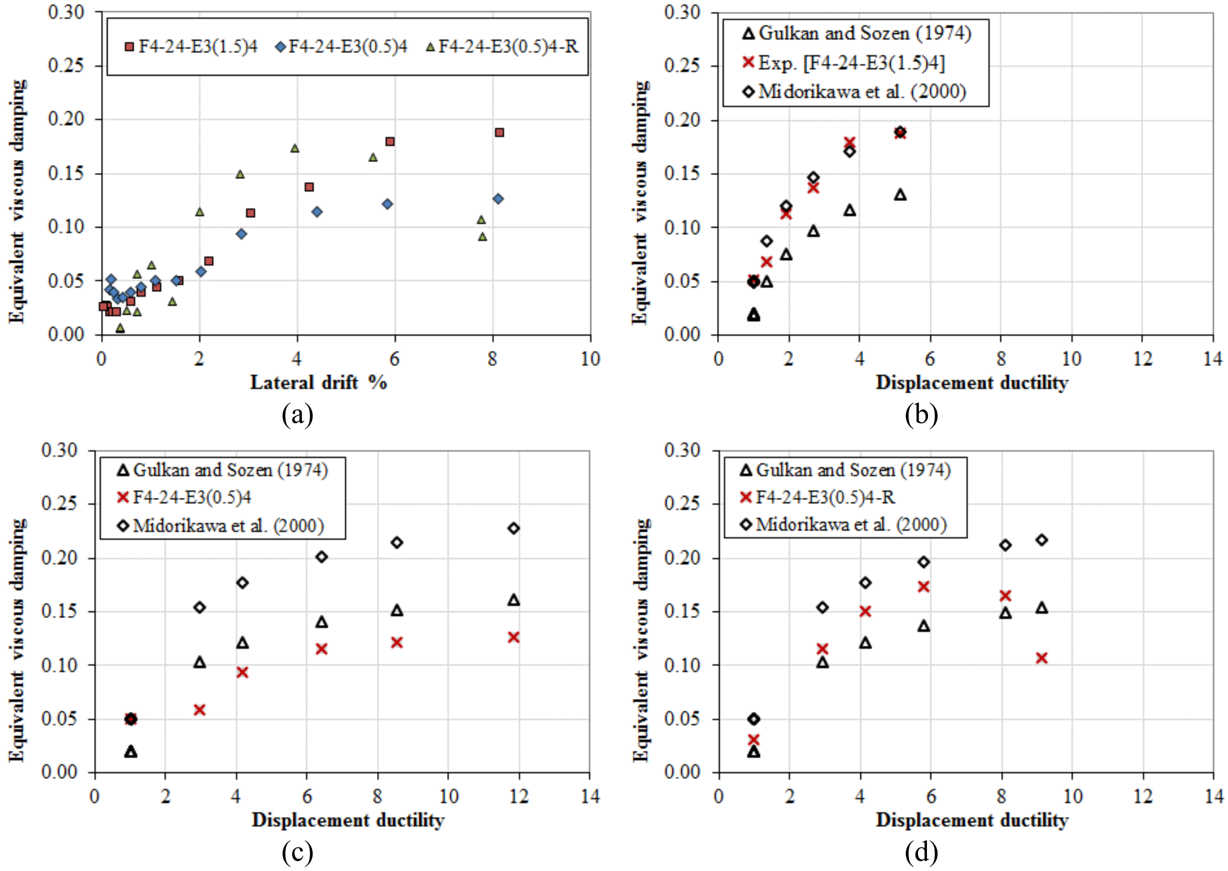

Fig. 21 – Equivalent viscous damping vs. displacement ductility for the tested HC-FCS columns (a) equivalent viscous damping vs. drift, (b) F4-24-E3(1.5)4, (c) F4-24-E3(0.5), and (d) F4-24-E3(0.5)4-R